ARTICLES
https://doi.org/10.1038/s42255-021-00390-y

nature metabolism

Single-cell metabolic imaging reveals a SLC2A3-dependent glycolytic burst in motile endothelial cells

David Wu[1,6], Devin L. Harrison[1,2,3,6], Teodora Szasz[4], Chih-Fan Yeh[5], Tzu-Pin Shentu[1], Angelo Meliton[1], Ru-Ting Huang[1], Zhengjie Zhou[1], Gökhan M. Mutlu[1], Jun Huang[2,3] ✉ and Yun Fang[1,2] ✉

Single-cell motility is spatially heterogeneous and driven by metabolic energy. Directly linking cell motility to cell metabolism is technically challenging but biologically important. Here, we use single-cell metabolic imaging to measure glycolysis in individual endothelial cells with genetically encoded biosensors capable of deciphering metabolic heterogeneity at subcellular resolution. We show that cellular glycolysis fuels endothelial activation, migration and contraction and that sites of high lactate production colocalize with active cytoskeletal remodelling within an endothelial cell. Mechanistically, RhoA induces endothelial glycolysis for the phosphorylation of cofilin and myosin light chain in order to reorganize the cytoskeleton and thus control cell motility; RhoA activation triggers a glycolytic burst through the translocation of the glucose transporter SLC2A3/GLUT3 to fuel the cellular contractile machinery, as demonstrated across multiple endothelial cell types. Our data indicate that Rho-GTPase signalling coordinates energy metabolism with cytoskeleton remodelling to regulate endothelial cell motility.

Endothelial cells exhibit motile behaviours in response to haemodynamics, during migration in angiogenesis and during contractions in barrier failure—each of which involves drastic morphological changes that require energy production and consumption. Bulk measurements have revealed that (1) endothelial cells preferentially utilize glycolysis for fuelling migration[1], (2) endothelial cells are dynamically regulated by shear stress[2–4] and (3) endothelial motilities are tightly regulated by the Rho family of small GTPases[5]. However, mechanistic coupling of motility to energy in typically heterogeneous cell populations requires simultaneous information at the single-cell level. Therefore, there is a critical need for single-cell metabolic measurements that can inform new mechanisms by linking cell motility phenotypes to energy production. Furthermore, measuring energy production in spatially disparate subcellular structures of a single cell is expected to provide mechanistic insight into cell biology because most cells dynamically regulate their metabolic programs as a result of nutrient availability, anabolic requirements and energy demand.

Using single-cell imaging analysis, we linked glycolysis to motility in individual endothelial cells in order to understand spatially heterogeneous phenomena. This Förster resonance energy transfer (FRET) image-based approach uses deep learning[6,7] to rapidly perform segmentaton and quantify intracellular glycolytic metabolites, including lactate, glucose, pyruvate and ATP in single endothelial cells, thus linking metabolic states to key endothelial motile phenotypes, including adaptation to shear stress, migration and contraction. A strong correlation between morphology and glycolytic rate at the single-cell level was identified, which was further confirmed by the subcellular distribution of high glycolytic rates at sites of active actin turnover. Our single-cell metabolic measurements discovered that the activation of GTPase RhoA triggers a glycolytic burst essential for the endothelial contractile machinery. We further discovered that glucose transporter SLC2A3/GLUT3 controls the RhoA-induced endothelial glycolysis and subsequent contraction. These results highlight the importance of single-cell metabolic analyses in their ability to uncover a new paradigm of small GTPase-dependent coupling of energy production to cell motility.

Results

Development of a single-cell metabolic imaging method. To study motile phenotypes of endothelial cells, we devised a method for quantifying the lactate concentration and glycolytic rate of individual cells. Here we transduced endothelial cells with Laconic, a FRET-based lactate biosensor comprising an mTFP–Venus FRET pair and the bacterial transcription factor LldR[8]. LldR binds lactate, causing the intramolecular distance between the members of the FRET pair to change, which leads to increased mTFP (acceptor)/Venus (donor) (or increased 1/FRET) signal. In this way, lactate concentrations are positively proportional to 1/FRET (Extended Data Fig. 1a). Laconic-expressing human endothelial cells were imaged, segmented using a semantic segmentation pipeline and assembled into fluorescence traces under biochemical and/or biomechanical stimulations (Fig. 1a). This allowed us to monitor the terminal metabolite in glycolysis, lactate, in endothelial cells, thus directly revealing endothelial glycolysis for energy production. A deep-learning approach with U-nets[7] using custom code in MATLAB rapidly and reliably performed pixel-level classification of images and segmentation of single cells, with a Boundary F_1

[1]Department of Medicine, Biological Sciences Division, The University of Chicago, Chicago, IL, USA. [2]Graduate Program in Biophysical Sciences, The University of Chicago, Chicago, IL, USA. [3]Pritzker School of Molecular Engineering, The University of Chicago, Chicago, IL, USA. [4]Research Computing Center, The University of Chicago, Chicago, IL, USA. [5]Division of Cardiology, Department of Internal Medicine and Cardiovascular Center, National Taiwan University Hospital, Taipei, Taiwan. [6]These authors contributed equally: David Wu, Devin L. Harrison. ✉e-mail: huangjun@uchicago.edu; yfang1@medicine.bsd.uchicago.edu

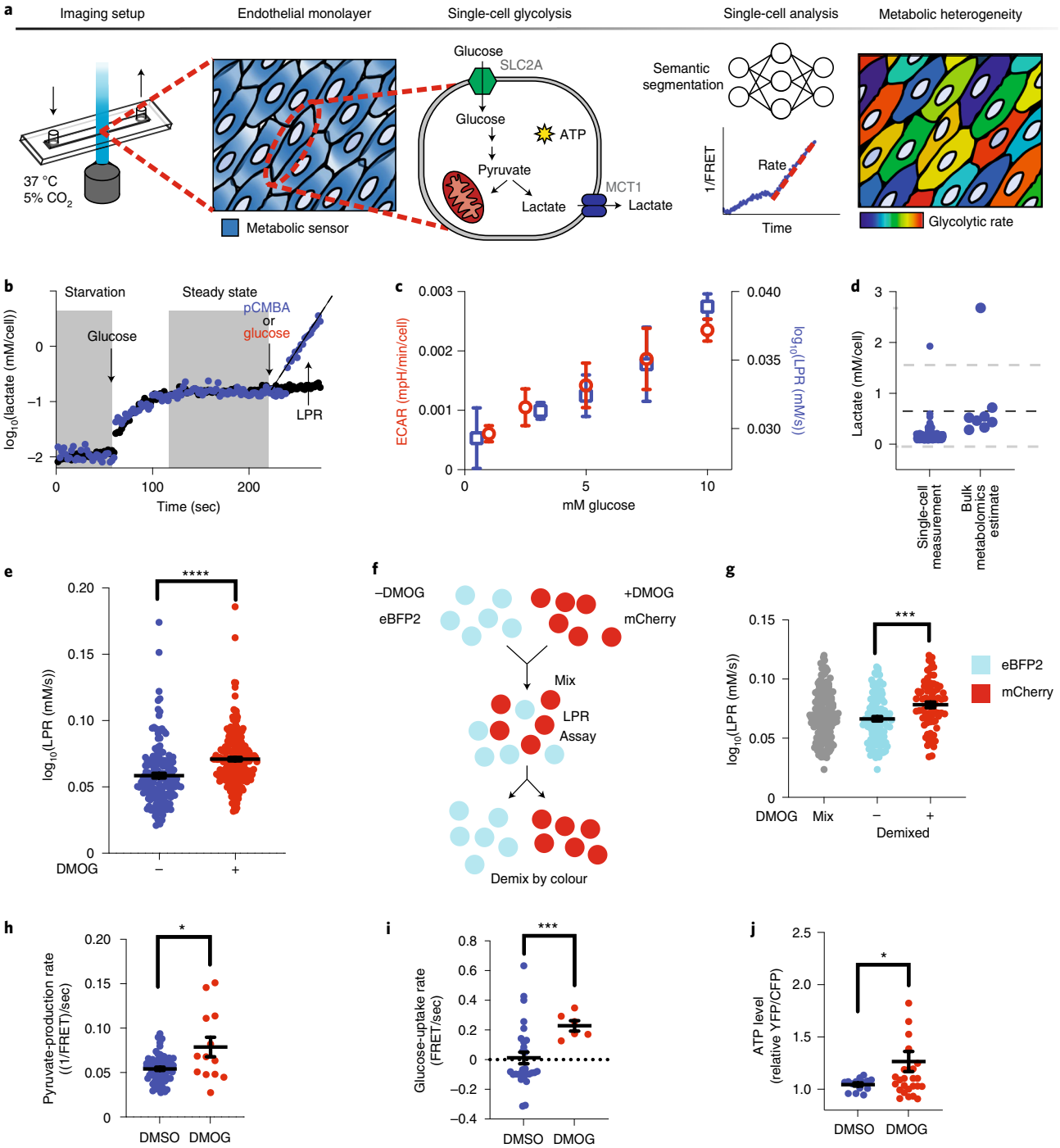

Fig. 1 | Single-cell LPR distinguishes metabolically heterogeneous subpopulations. a, Schematic of single-cell metabolism quantification by deep learning. Endothelial cells were plated into imaging chambers capable of fluid exchange with controlled temperature and CO_2. Once endothelial cells grew to form a monolayer, metabolite sensors were genetically introduced to measure glycolysis. Within each cell, glucose is converted to pyruvate and consumed by mitochondria or fermented into lactate and exported via MCT1, thus generating ATP. Deep-learning-enabled semantic segmentation was used for linking cells into a 1/FRET time series for quantification of intracellular lactate production over time to reveal metabolic heterogeneity. **b**, Following starvation, glucose was injected, followed by glucose and MCT1 inhibitor pCMBA (blue dots) or glucose alone (black dots). The slope (black dotted line) of each cell is the LPR, filtered for fitting with R^2 values ≥ 0.9. **c**, Single-cell LPR (blue) and per-cell ECAR (red) versus extracellular glucose concentration ($n = 7$, 226, 43, 200, 206 cells for LPR left to right, $n = 4$, 3, 4, 3, 3 wells for ECAR left to right; error bars are s.e.m.). **d**, Comparison of steady-state lactate levels ($n = 167$ cells) with metabolomics ($n = 8$). The dotted black line is the mean metabolomics ($n = 8$) estimate of intracellular lactate measured by mass spectrometry. Grey dotted lines are s.d. of metabolomics. **e**, LPR of vehicle DMSO-treated (–) or DMOG-treated (+) endothelial cells ($n = 164$ –, 256 +; error bars are s.e.m., $P < 0.0001$). **f**, eBFP2 or mCherry cells were treated with DMSO or DMOG, then mixed and imaged together. **g**, Following the steps in **f**, the LPR was then deconvoluted by colour ($n = 166$ eBFP2, $n = 79$ mCherry; error bars are s.e.m., $P < 0.0001$). **h**–**j**, Pyruvate-production rate (**h**, $n = 67$, 13, $P = 0.048$), glucose-uptake rate (**i**, $n = 29$, 6, $P = 0.0005$) and ATP levels (**j**, $n = 14$, 29, $P = 0.0323$) in single HAECs treated overnight with DMSO or DMOG measured using genetically encoded sensors. Error bars are s.e.m. Statistical significance was determined by two-sided Welch's *t*-test. $^*P \leq 0.05$; $^{***}P \leq 0.0005$.

Table 1 | Deep learning semantic segmentation metrics

Matthew's correlation coefficient			**0.85**	
Global accuracy			**0.84**	
Class	**Background**	**Cytoplasm**	**Nuclei**	**Cell boundary**
Class-specific accuracy	0.85	0.83	0.45	0.78
s.d. of accuracy	0.083	0.079	0.086	0.055
Boundary F_1 score	0.96	0.95	0.75	0.94
s.d. of boundary F_1 score	0.05	0.047	0.079	0.071
Precision	0.85	0.83	0.45	0.78
Recall	0.97	0.84	0.31	0.38
Dice score	0.9	0.82	0.38	0.53
s.d. of Dice score	0.074	0.0659	0.064	0.064

score[9] (which measures how closely the predicted boundary of an object matches the ground-truth boundary) for identifying the cytoplasm of >90%, and class-specific cytoplasm accuracy, precision, recall and Dice score (which measures the overlap between two segmented images) all >80% (Extended Data Fig. 1b and Table 1). Single-cell fluorescence following segmentation was highly correlated with ground-truth fluorescence (Extended Data Fig. 1c).

To reliably measure and calibrate physiological levels of intracellular lactate and glycolysis using Laconic, we controlled intracellular lactate concentrations by permeabilizing human aortic endothelial cells (HAECs) and subjecting them to different concentrations of lactate. As shown in Extended Data Fig. 1a, the 1/FRET change is linear to 6 orders of magnitude of log (lactate concentration) ($R^2 = 0.96$). However, lactate export is a dynamic process in live cells that is regulated by the concentration gradient between the extra- and intracellular compartments[10]. Thus, in order to measure the glycolytic rate of a cell, lactate export was blocked through inhibition of monocarboxylate transporter 1 (MCT1), the major lactate transporter in endothelial cells[11] (Fig. 1a). Upon MCT1 blockade by *p*-chloromercuribenzoic acid (pCMBA), we observed a continuous increase of lactate in individual cells, the slope of which we defined as the lactate-production rate (LPR) (Fig. 1b), which reflects the overall glycolytic rate in a single endothelial cell. Furthermore, the single-cell LPR increased linearly, in agreement with bulk extracellular acidification measurements, as a function of extracellular glucose concentration (Fig. 1c). Employing a bootstrap algorithm simulating LPR, by drawing from ground-truth fluorescence values and fitting slopes to the deep-learning-measured fluorescence (Extended Data Fig. 1c), we estimated that the absolute quantification error of LPR was 5% (Methods and Extended Data Fig. 1d).

Consistently, the steady-state intracellular concentration of lactate measured by single-cell FRET was within the range estimated by bulk mass spectrometry (~0–1.6 mM) (Fig. 1d). Corresponding to single-cell LPR, blockade of MCT1 with pCMBA[10] also reduced extracellular acidification in a bulk bioenergetics flux assay (Extended Data Fig. 2a). Additionally, we were able to increase intracellular lactate at the single-cell level with glucose or oligomycin stimulation, and inhibit lactate production by 2-deoxyglucose, similarly to an extracellular-flux-based glycolysis stress test at the bulk level (Extended Data Fig. 2b).

To test the LPR's ability to distinguish heterogeneous glycolytic rates in cell populations, which is critical for differentiating subpopulations, we mimicked hypoxic conditions in endothelial cells by treating them with dimethyloxaloylglycine (DMOG). DMOG inhibits prolyl hydroxylase, thereby promoting the stabilization of transcription factor hypoxia inducible factor-1α (HIF-1α)[2]. We found that the single-cell LPR was elevated in DMOG-treated cells (Fig. 1e), in agreement with an increase in ECAR measured in bulk extracellular flux (Extended Data Fig. 2c). We next forced metabolic heterogeneity by mixing vehicle (DMSO)- or DMOG-treated cells that were previously labelled with either eBFP2 or mCherry fluorescent proteins, respectively (Fig. 1f). By assessing the LPR of each cell and then demixing by colour (Fig. 1g), our method distinguished authentic metabolic subpopulations.

In addition to lactate, we further employed other genetically encoded FRET-based sensors to measure key glycolytic metabolites, including pyruvate[12], glucose[13] and ATP[14], to cross-validate these findings with DMOG. Pyruvate production, glucose uptake and ATP levels were all increased in DMOG-treated cells relative to controls treated with DMSO (Fig. 1h–j). Notably, pyruvate and glucose have alternative fates, and ATP is not exclusively produced by glycolysis, whereas lactate production is a definitive surrogate for glycolysis. These findings validated our primary results using the Laconic sensor, and laid a solid foundation for the general application of our single-cell method to study metabolism-linked cell phenotypes.

Glycolytic rates of single cells subjected to flow. We then assessed single-cell glycolytic heterogeneity in a spatial context by exploiting the haemodynamic-flow-dependent activation of endothelial cells, which are generally subject to different shear stresses depending on the local flow conditions in the vasculature[15]. Disturbed flow-induced cell activation leads to atherosclerosis at arterial branch points[15], driven by endothelial glycolysis induced by low shear stress[2,3], and abrogated by high shear stress, which is known to repress glycolysis through reducing the expression of a key glycolytic enzyme, PFKFB3, in a manner dependent on transcription factor KLF2 (ref. [4]). However, the ability to study flow-induced metabolic changes has so far been limited to extracellular flux without spatial resolution[2].

Using a cone and plate device to generate spatially heterogeneous shear forces over microscopic distances (Fig. 2a), we focused on an area at the flow boundary (indicated by endothelial elongation and alignment; Fig. 2b) to determine force-dependent metabolic rates. As shown in Fig. 2c, cells subjected to high shear stress had a reduced LPR compared with that of those exposed to low shear stress, consistent with our previously published bulk data as measured by ECAR[2]. We next linked metabolism to a morphological phenotype (flow-induced endothelial cell elongation) at the single-cell level. By analysing endothelial cells exposed to shear stress, we found a direct association between force-induced cell morphology and glycolytic rate. We plotted the LPR and shear stress as a function of cell length and found a negative correlation with LPR but a positive correlation with shear stress (Fig. 2d). At ×20 magnification, cell length is strongly negatively correlated with LPR (Fig. 2e,f). This result was partially caused by the presence of external forces (shear

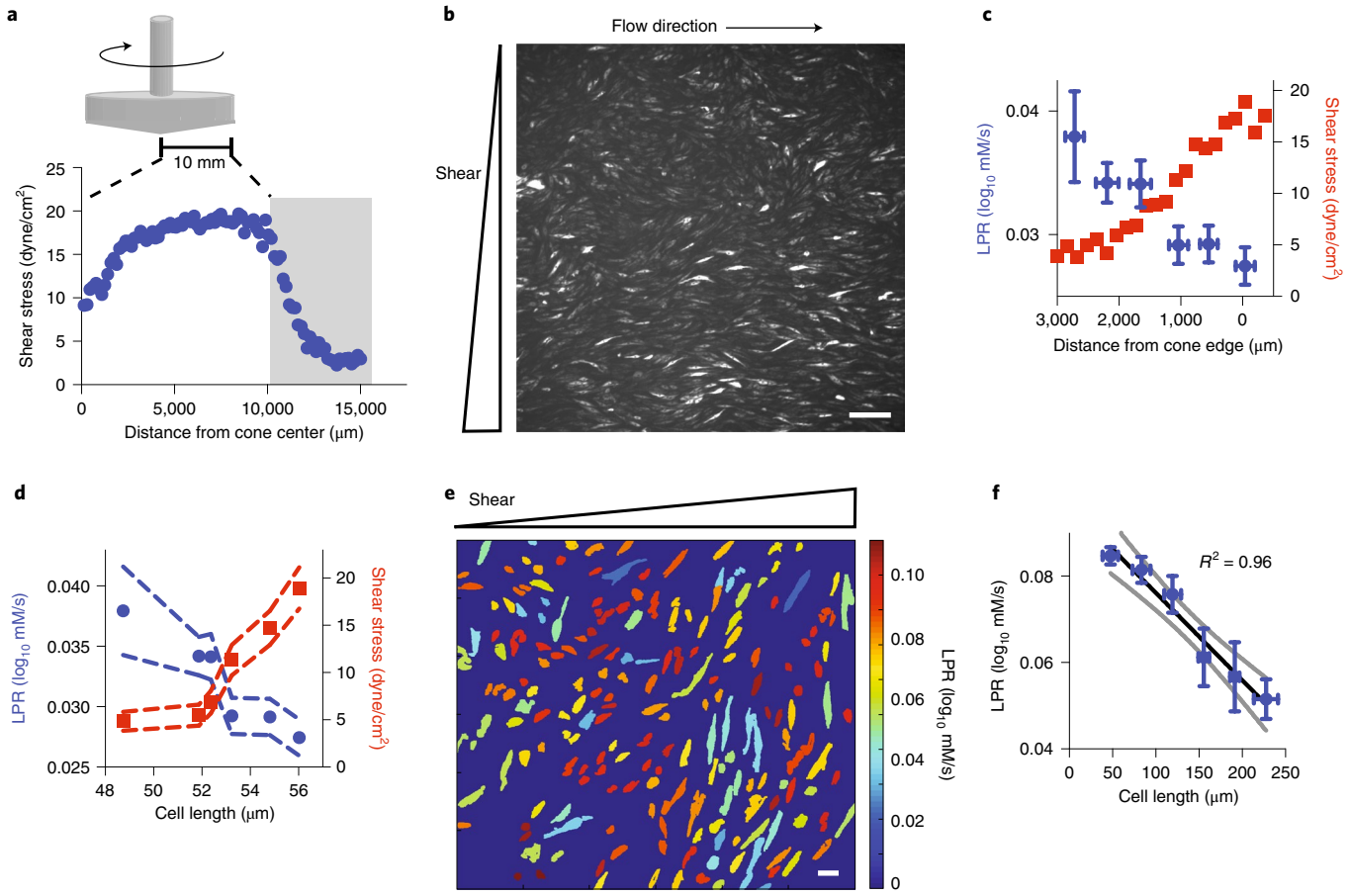

Fig. 2 | Endothelial LPR in response to shear stress is heterogeneous. a, A cone and plate device was used to generate shear stress, as measured by particle image velocimetry, with the grey bar indicating the area of interrogation. **b**, The corresponding Laconic fluorescence image at the grey zone in **a**. Scale bar, 165 μm (representative of $n = 3$ biological replicates). **c**, LPR (blue) and shear stress (red) versus distance from cone edge ($n = 27, 47, 34, 34, 35, 33$ left to right; error bars are s.e.m.). **d**, Replot of **c**, with LPR (blue) and shear stress (red) as a function of cell length; error bars are s.e.m. **e**, The LPR of segmented endothelial cells subjected to flow (colour from blue to red indicates the increase of LPR in each cell). Scale bar, 44 μm. **f**, Length of major axis of endothelial cells (in **e**) plotted against measured LPR (cell number $n = 103, 47, 18, 8, 8, 4$ low to high cell length; error bars are s.e.m.); s.d. of regression coefficients for R^2 for **f** is 0.074.

stress), which could change metabolic rates independently of cell morphology; however, shorter cells within the high-shear-stress region exhibit a higher LPR (Fig. 2e).

Glycolysis fuels the migration of single endothelial cells. Endothelial cells migrate during angiogenesis or wound closure. This process requires energy, involves dramatic changes in cell shape and is dependent on RhoA–ROCK-1 remodelling of the actin cytoskeleton[5]. In typical wound assays, single-cell migrations are heterogeneous: some cells are motile, while others remain stationary[16]. It has been shown that endothelial cell migration requires glucose, whereas endothelial cell growth requires glutamine usage in oxidative phosphorylation[1,17]. However, it is not known whether individual migrating cells are more glycolytic than stationary cells, which could elucidate whether metabolism is a driver of heterogeneous cell migration in a disrupted cell monolayer. We first demonstrated that glucose is necessary for migration whereas mitochondrial metabolism is dispensable for wound closure (treatment with Antimycin A, Fig. 3a). The results indicated that cell migration is driven by glycolysis. In accordance, HAECs treated with DMOG, which increases glycolytic capacity in an HIF-1α-dependent manner[18], enhanced migration and are able to close wounds faster than control (Fig. 3b).

However, it remains unknown whether individual cells that migrated further were more glycolytic, as activation of HIF-1α by DMOG could turn on thousands of genes[2]. In order to elucidate whether cell glycolysis fuels individual cell motility, we applied single-cell metabolic assays to analyse migrating endothelial cells in a wound assay. By tracking individual cell migrations (Fig. 3c) over the course of 48 hours, we confirmed that, overall, cells in the more stationary 'tissue' migrated less than cells in the more migratory 'wound' (Fig. 3d). We found that migratory cells, cells that travelled more than one cell length, were more glycolytic than were stationary cells (Fig. 3e). We further found that cell migration distance is positively correlated with cell glycolysis (Fig. 3f), regardless of the final cell positions in the tissue or wound regions. These results suggest that the migration of endothelial cells is fuelled by glycolysis, which is moreover proportional to work performed.

RhoA activation increases endothelial glycolysis. Having shown that glycolysis fuels cell migration, we next quantified the glycolytic rate during cell contraction, a key motile endothelial process that occurs over a short timespan (minutes) and is thus independent of transcriptional control. Because GTPase RhoA activation is central to inducing the contractile apparatus of endothelial cells within minutes[19], we hypothesized that controlled RhoA agonism

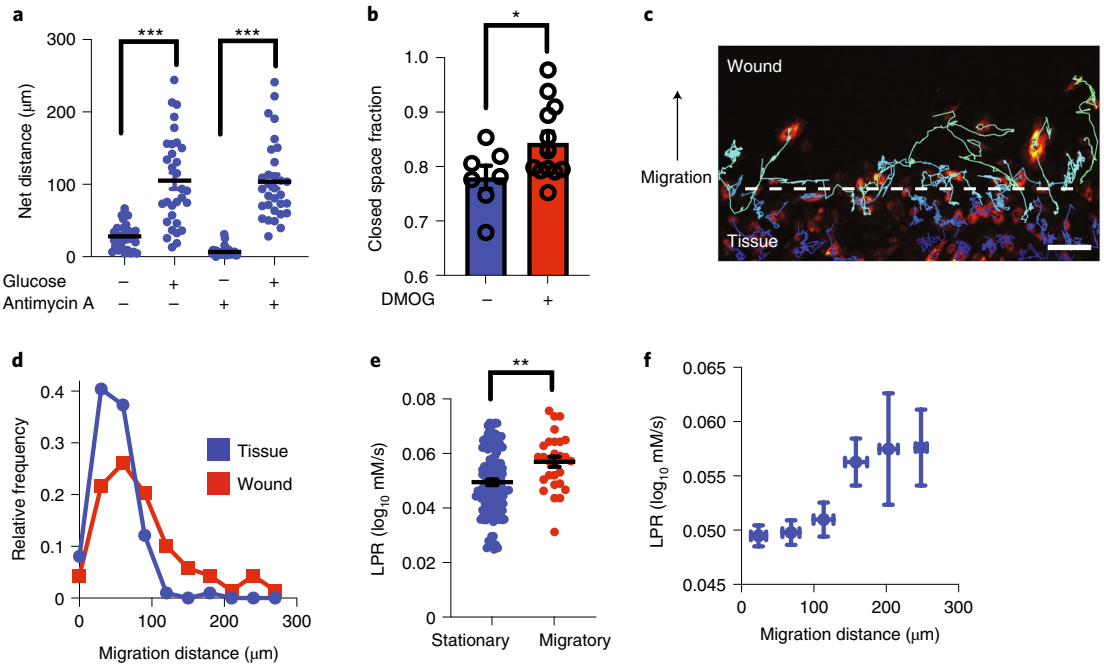

Fig. 3 | Single-cell metabolism links migratory cell phenotypes to glycolysis states. a, Migration distance of HAECs with or without glucose and with or without antimycin A ($n = 31$ cells each condition; error bars are s.e.m., $P < 0.0001$ for both pairs of conditions). **b**, Migration scratch assay quantification with and without DMOG treatment ($n = 7$ and 12, respectively; error bars are s.e.m., $P = 0.0474$). **c**, Migrating endothelial cells (false colour) were tracked for 48 hours following wound formation. Scale bar, 150 μm. **d**, Frequency distribution of cell migration distance after 48 hours in the wound versus in tissue. **e**, The LPR of cells that migrated less than 50 μm compared with cells that migrated more than 200 μm (cell number $n = 141$ and 28, respectively; error bars are s.e.m., $P = 0.0012$). **f**, The LPR change as a function of cell migrated distance ($n = 114$, 118, 42, 12, 8, 8 from low to high migration distance; error bars are s.e.m.). Statistical significance was determined by two-sided Welch's *t*-test. $^*P \leq 0.05$; $^{**}P \leq 0.005$; $^{***}P \leq 0.0005$.

would induce a glycolytic burst to power cell contractions. RhoA activation or inactivation in HAECs was achieved by overexpressing constitutently active RhoA (RhoA-Q63L) or dominant negative RhoA (RhoA-T19N). As shown in Fig. 4a, RhoA-Q63L, compared with RhoA-T19N, increased single-cell LPR. To remove possible batch effects, we next conjugated fluorescent protein eBFB2 to RhoA-T19N and fluorescent protein mScarlet-i to RhoA-Q63L, followed by cell mixing and single-cell LPR measurements. Deconvolution by colour showed significantly increased glycolysis in RhoA-activated (mScarlet-i positive) HAECs compared with that in RhoA-inactivated (eBFP2 positive) cells (Fig. 4b). Switching fluorescent labelling of RhoA-Q63L and RhoA-T19N had no effect on the results (Extended Data Fig. 3a). We next treated HAECs with lysophosphatidic acid (LPA), another well-known RhoA agonist[20], which significantly increased single-cell LPR compared with that of untreated controls (Fig. 4c). Furthermore, treatment with thrombin, a serine protease that rapidly stimulates RhoA and subsequently RhoA kinase-1 (ROCK-1)[21] to produce contractions and barrier breakdown, significantly increased LPR in 7 minutes, which was largely abrogated by treatment with a specific ROCK-1 inhibitor, Y27632 (Fig. 4d). In accordance, glucose uptake and ATP levels were also elevated shortly after thrombin treatment (Fig. 4e). Thus, activation of GTPase RhoA causatively drives intracellular lactate production and glycolysis in single endothelial cells.

RhoA activates contractile machinery through glycolysis. Because the activity of RhoA-dependent kinases requires ATP, we hypothesized that the downstream functions of RhoA–ROCK-1 are dependent on glycolysis. RhoA–ROCK-1 activation causes rapid phosphorylation of cofilin (CFL), which enacts reorganization of the actin cytoskeleton from cortical actin to stress fibres[19,22]. RhoA–ROCK-1 activity also causes phosphorylation of myosin light chain (MLC), which actively pulls on stress fibres, causing cell contractions and intercellular gaps in endothelial monolayers (failure of the endothelial paracellular barrier) as well as the reduction in monolayer impedance[23–25]. Phosphorylation of CFL and MLC occurs in 2–30 minutes with relaxation of the cell to its basal state after 1 hour as the stimulus is depleted[19,21]. To test our hypothesis, we used the hexokinase inhibitor 2-deoxyglucose (2DG) to block glycolysis. Indeed, 2DG significantly reduced basal CFL and MLC phosphorylation in HAECs; moreover, it completely blocked thrombin-induced phosphorylation of CFL and MLC (Fig. 4f), demonstrating that RhoA–ROCK-1 downstream effects are dependent on active glycolysis. Consistently, the degree of contraction, or change in monolayer impedance, was dependent on the concentration of glucose in the medium, as measured by transendothelial electrical resistance (TEER) (Fig. 4g). Concordantly, depleting endothelial glycolysis with 2DG also prevented thrombin-induced barrier failure by TEER (Fig. 4h). Furthermore, cells in which ROCK-1 was inhibited with Y27632 followed by thrombin treatment mimicked the phenotype of those that were pretreated with 2DG (Extended Data Fig. 3b). These data collectively demonstrate that RhoA–ROCK-1-dependent glycolysis is required for the contractile machinery of endothelial cells.

RhoA simulates contractions via glucose transporter SLC2A3. We next determined the molecular mechanisms by which RhoA induces glycolysis to stimulate endothelial contraction. Since the increase in glycolysis occurs over a short timespan (measured at 7 minutes) following RhoA activation (Fig. 4d) and availability of glucose determines the degree of downstream phosphorylation and contraction (Fig. 4f,g), we hypothesized that glucose uptake plays a critical role in RhoA-induced glycolysis. Previous studies have shown that SLC2A1/GLUT1 is a major glucose transporter

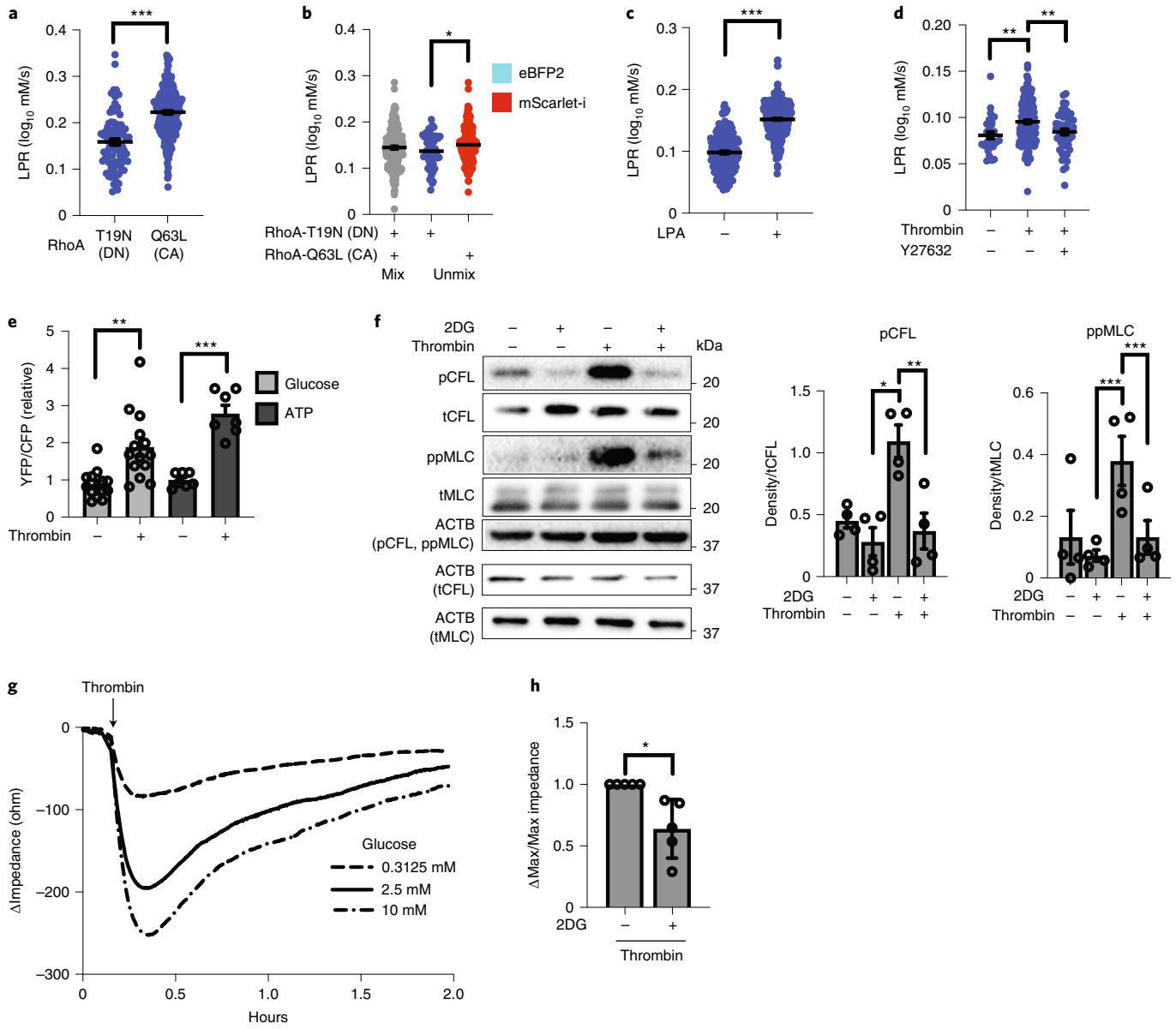

Fig. 4 | Single-cell imaging of lactate production reveals RhoA drives endothelial cell glycolysis, which is necessary for contractions. a, LPR of HAECs transfected with either RhoA-T19N (dominant negative (DN) form) or RhoA-Q63L (constitutively active (CA) form) ($n = 91, 250$, respectively, $P < 0.0001$). **b**, RhoA-Q63L-mScarlet-i transfected ECs have increased LPR compared with those transfected with RhoA-T19N-eBFP after unmixing by color ($n = 52, 174$, respectively, $P = 0.0193$). **c**, LPR of HAECs treated with control (DMSO (-)) or 10 μm of lysophosphatidic acid (LPA) (+) for 30 min ($n = 244$ and 423, respectively; $P < 0.0001$). **d**, Thrombin-induced LPR ($n = 171$) compared with untreated control ($n = 28$, $P = 0.0028$), which is suppressed by Y27632 ($n = 51$, $P = 0.0042$). **e**, Glucose and ATP levels before and after treatment with thrombin, measured by FRET ($n = 14$ cells glucose, $P = 0.0012$; $n = 7$ cells ATP; $P = 0.0001$). **f**, Western blot of 2DG pretreatment in the presence or absence of thrombin and phosphorylation of cofilin (pCFL) and MLC (ppMLC) ($n = 4$ biological replicates). For pCFL, $P = 0.008$ for thrombin versus 2DG and $P = 0.0038$ for thrombin versus thrombin + 2DG. For ppMLC, $P < 0.0001$ for both thrombin versus 2DG and thrombin versus thrombin + 2DG). Loading control (ACTB) for each protein is noted in parentheses. pCFL/ACTB is normalized to total cofilin (tCFL/ACTB). ppMLC/ACTB is normalized to total MLC (tMLC/ACTB). **g**, TEER trace of HAECs after thrombin treatment in different extracellular glucose concentrations. **h**, Inhibition of hexokinase with 2DG reduces thrombin-induced permeability, as measured by TEER ($n = 5$ each, biological replicates; $P = 0.0283$). Statistical significance determined by two-sided Welch's *t*-test (**a**–**c**,**e**,**h**) or by one-way ANOVA followed by Bonferroni test (**d**,**f**). All error bars are s.e.m. $^*P \leq 0.05$; $^{**}P \leq 0.005$; $^{***}P \leq 0.0005$.

in endothelial cells. SLC2A1 contributes to the basal endothelial glycolytic capacity in the blood–brain barrier[26] and pulmonary vasculature[27], as well as to increased glycolysis stimulated by chronic (hours) exposure to hypoxia and disturbed flow in large arteries[2]. We therefore first tested the role of SLC2A1. Unexpectedly, small interfering RNA (siRNA)-mediated *SLC2A1* knockdown did not reduce thrombin-induced phosphorylation of CFL and MLC in HAECs (Extended Data Fig. 4a). At the same time, quantitative reverse transcription PCR (qRT–PCR) analysis identified that *SLC2A3* is the most abundant glucose transporter transcript in HAECs (Extended Data Fig. 4b). We therefore tested the role of SLC2A3 in RhoA-induced glycolysis. Our data showed that

SLC2A3 knockdown by siRNAs reduced basal phosphorylation of CFL and MLC and significantly abrogated thrombin-induced phosphorylation of CFL and MLC with three separate siRNAs (Fig. 5a and Extended Data Fig. 4c,d).

Although *SLC2A3* knockdown had no effect on basal endothelial glycolysis, it largely abolished the thrombin-induced glycolytic burst, as detected by single-cell LPR (Fig. 5b). In direct comparison, *SLC2A1* knockdown led to a measurable decrease in LPR after thrombin stimulation, but this decrease was far less than that following *SLC2A3* knockdown (Extended Data Fig. 4e). Consistently, the thrombin-induced increase in glucose and ATP levels was abrogated by *SLC2A3* knockdown (Extended Data Fig. 4f,g). Because the glycolytic burst could not be attributed to *SLC2A3* transcriptional regulation given the acute response (measured within 7 minutes), we hypothesized that SLC2A3 is regulated post-transcriptionally by RhoA–ROCK-1. To test this hypothesis, we performed immunofluorescence imaging of SLC2A3 in thrombin-treated HAECs. Using total internal reflection fluorescence (TIRF) microscopy, which selectively illuminates membrane fluorophores close to the cover slip (within ~100 nm)[28,29], we detected significantly increased intensity of SLC2A3 in granules near the plasma membrane of single HAECs following thrombin stimulation; such accumulation of SLC2A3 was abrogated by ROCK inhibitor Y27632, further suggesting the involvement of the Rho–ROCK signalling pathway (Fig. 5c,d). In agreement with the SLC2A3-dependent glycolytic burst and phosphorylation of CFL and MLC, thrombin-induced endothelial contraction was significantly abrogated by *SLC2A3* knockdown, demonstrated by increased monolayer impedance by TEER (Fig. 5e) and reduced intercellular gap size (gap size index, Fig. 5f), although the number of gaps was unchanged (gap index, Extended Data Fig. 4h)[30]. Furthermore, increasing the amount of extracellular glucose increased gap size and gap number, which was blunted by *SLC2A3* knockdown (Extended Data Fig. 4i). Contraction (gap size index), but not gap number, was partially rescued under *SLC2A3* knockdown by treatment with oligomycin to divert all glucose to be utilized via glycolysis (Extended Data Fig. 4j). Thrombin-induced phosphorylation of CFL and MLC were also significantly abrogated by *SLC2A3* knockdown in human umbilical endothelial cells (HUVECs) (Extended Data Fig. 5a) and human lung microvascular cells (HMVECs) (Extended Data Fig. 5b). Thrombin-induced HUVEC contractions (as measured by cell size, Extended Data Fig. 5c) and HMVEC contractions (as measured by intercellular gaps, Extended Data Fig. 5d) were also significantly reduced by *SLC2A3* knockdown, indicating that this pathway is conserved across multiple endothelial cell types.

The functional role of SLC2A3 in endothelial glycolysis and contraction is largely unknown. In order to explore the in vivo relevance of SLC2A3 in barrier regulation, we needed to first ascertain the expression profile of *Slc2a1* and *Slc2a3* in primary endothelial from different organs in mice. Gene Expression Omnibus datasets (GEOD) were downloaded from EndoDB, a database of curated endothelial transcriptomics datasets[31]. As shown in Extended Data Fig. 6a, *Slc2a3* has expression levels similar to *Slc2a1* across multiple organs (normalized to *Slc2a1*). We next overexpressed *SLC2A3* under the endothelial-specific *CDH5*/VE-cadherin promoter and evaluated vascular leak in mouse aortas. Mouse aortas, because of their intrinsic curvature, exhibit RhoA activation due to hemodynamic shear forces[32]. We employed a delivery system that integrates polyethylenimine (PEI) nanoparticles and plasmids with the endothelial-specific *CDH5*/VE-cadherin promoter. Intravenous injection of *CDH5*-driven, mScarlet-i-expressing plasmids resulted in mScarlet-i fluorescence in arterial endothelium, highlighted by colocalization with Cdh5/ve-cadh (which marks endothelium) adjacent to the lumen, but not the underlying medium and adventitia (yellow signal in merge panel, Extended Data Fig. 6b), demonstrating endothelial-specific overexpression in mice. The same approach using *CDH5*-driven, *SLC2A3*-expresssing plasmids led to *SLC2A3* overexpression in the aortic endothelium, measured by qRT–PCR (Extended Data Fig. 6c), but not in the medium or adventitia in mice. To demonstrate functional relevance of SLC2A3, mice were injected with PEI nanoparticles containing *CDH5-SLC2A3* or *CDH5*–Ctrl plasmids 24 hours prior to euthanization. One hour prior to euthanization, Evans blue dye was injected retro-orbitally. Evans blue dye binds to albumin and transits the endothelial barrier in a paracellular fashion under conditions of diminished tight and adherent junctions and quantitatively measures the leakiness of mouse aortas[33]. Endothelial overexpression of *SLC2A3* results in leakiness of the aorta, as quantified by Evans blue spectroscopy (OD_{620}), normalized to aorta weight after dye extraction (Extended Data Fig. 6d). This experiment suggests that SLC2A3 regulates the endothelial barrier in vivo. Collectively, these results demonstrate the importance of SLC2A3 for fuelling RhoA–ROCK-1 downstream phosphorylation targets, and its importance in both in vitro and in vivo barrier function.

Subcellular glycolysis and cytoskeletal remodelling overlap. After finding that RhoA activation induces endothelial glycolysis and contraction within minutes at the single-cell scale (Fig. 4a–d), we sought to evaluate how glycolysis relates to morphological changes within individual endothelial cells at subcellular resolution. Reasoning that actin remodelling is dependent on high-energy phosphates, we hypothesized that localized changes in actin are correlated with glycolytic activity at the subcellular spatial scale. To test this hypothesis, we again stimulated actin remodelling with the RhoA agonist thrombin. By coexpressing Laconic and Lifeact–RFP[34] (an F-actin label) in endothelial cells, we measured LPR and actin remodleling in single endothelial cells with subcellular resolution at ×40 magnification (Fig. 6a). Lifeact signal increases and shimmers at the edges of thrombin-induced contracting cells, indicating active actin remodelling. In order to visualize actin remodelling, we computed the maximum intensity projection of the difference in Lifeact signals in the 7 minutes following thrombin addition prior to performing the LPR assay (Fig. 6a, difference image). The LPR image was captured by performing pixel-wise calculation of the slope of the FRET signal after addition of pCMBA (Fig. 6a, LPR). As shown in the merged image, the LPR signal was spatially correlated with the Lifeact difference image (Fig. 6a, LPR+difference and LPR+difference+nucleus). The Lifeact difference and LPR images together demonstrated enhancement of signals on the contracting edge and centre of the cell. To quantify the correlation, we calculated the degree of overlap using Manders' overlap coefficient (MOC) and Pearson's correlation coefficient (PCC). Thrombin-stimulated cells showed much higher levels of correlation between subcellular LPR and Lifeact than did those nonstimulated cells (Fig. 6b). This correlation was diminished by inhibition of ROCK (Y27632), actin polymerization (Latrunculin B) and myosin II (para-amino-Blebbistatin) (Fig. 6b). Moreover, *SLC2A3* knockdown reduced the correlation between Lifeact difference and LPR after thrombin treatment, indicating that RhoA-dependent SLC2A3 activity is necessary for the co-occurrence of subcellular glycolysis and actin remodelling (Fig. 6c).

Similarly, we assessed subcellular glycolysis using Laconic in migrating endothelial cells. Here, we computed the Lifeact difference image in the 10 minutes prior to performing the LPR assay (Extended Data Fig. 7a, difference image). In migrating HAECs, we found that LPR and Lifeact difference were significantly correlated (Extended Data Fig. 7a), compared with in controls (performed by randomizing the LPR images 10,000 times and computing the MOC or PCC) (Extended Data Fig. 7b). These results indicate that spatial cytoskeletal remodelling and glycolysis are correlated in multiple types of endothelial motilities.

To determine whether subcellular LPR was spatially related to RhoA, we next evaluated RhoA activity using a FRET-based biosensor

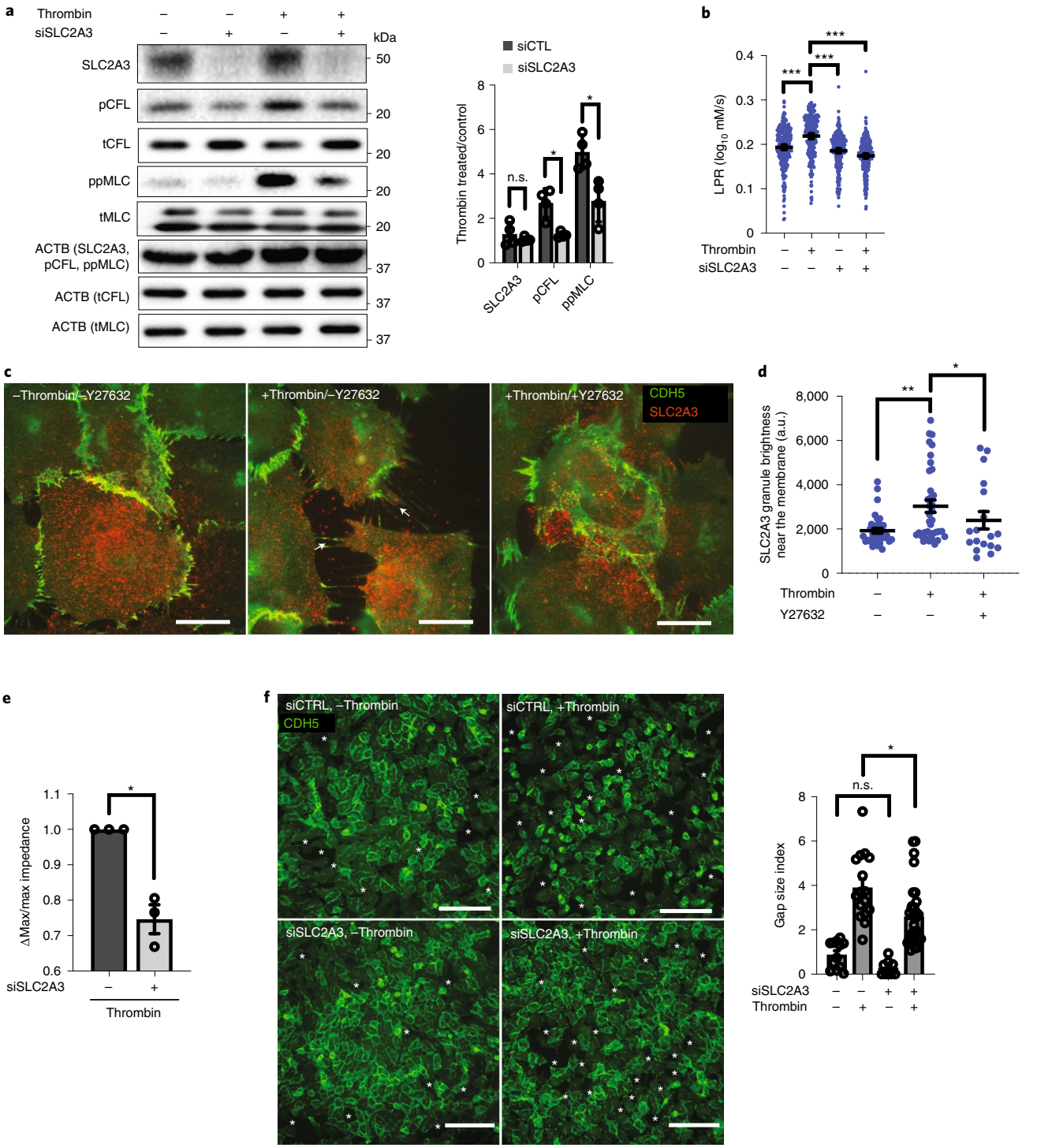

Fig. 5 | RhoA induces glucose transporter SLC2A3 translocation which drives subcellular glycolysis in thrombin-stimulated contractile endothelial cells. **a**, Western blot of phospho-cofilin and phospho-MLC in the presence or absence of siRNA targeted at *SLC2A3* and thrombin treatment ($n = 4$ biological replicates for all, $P = 0.0140$ for pCFL and $P = 0.0233$ for ppMLC). Loading control (ACTB) for each protein is marked with parentheses. Phosphoproteins are additionally normalized to total. **b**, LPR of siRNA targeted at *SLC2A3* or control with and without thrombin treatment ($n = 277, 263, 275, 278$ from left to right, $P < 0.0001$ for all comparisons). **c**, Representative immunofluorescence of membrane markers CDH5 (green) and SLC2A3 (red) in thrombin-treated cells causes SLC2A3 granule localization to membrane spikes, which is inhibited by Y27632, by TIRF microscopy. Scale bar, 5 µm. **d**, Quantification of SLC2A3 granule brightness near the membrane of **c** (a.u. ,arbitrary units; $n = 36, 36, 17$ images from left to right; $P = 0.003$ for thrombin versus control and $P = 0.0499$ for thrombin versus thrombin + Y27632). **e**, TEER measurement of thrombin-induced permeability changes in the presence or absence of siRNA targeted at *SLC2A3* ($n = 4$ biological replicates; $P = 0.0248$). **f**, Representative immunofluorescence of CDH5 and intercellular gaps, as quantified by gap size index, in HAECs treated with control or siRNA targeted at *SLC2A3* followed by thrombin treatment ($n = 12$ (top left), 16 (top right), 8 (bottom left), 32 (bottom right) images; $P = 0.0184$). Scale bars, 150 µm. Statistical significance determined by multiple unpaired two-tailed *t*-test, with multiple comparisons adjustment by the Holm–Šídák method (**a**), two-sided Welch's *t*-test (**e**,**f**) or by one-way ANOVA followed by Bonferroni test (**b**,**d**). All error bars are s.e.m. n.s., not significant. $^{*}P \leq 0.05$; $^{**}P \leq 0.005$; $^{***}P \leq 0.0005$.

RhoA–Flare[35] in single contractile endothelial cells. We found enhanced RhoA activity and increased LPR colocalized in similar areas following thrombin stimulation: the centre of the cells (Fig. 6d) as well as along the edges of the contractile aspects of the cell (Fig. 6d–f and Extended Data Fig. 7c–l). In contrast, where the cell edge did not move, there was no FRET (RhoA activity) (Extended Data Fig. 7i). Edges with persistent contraction consistently demonstrated high RhoA–Flare FRET (Extended Data Fig. 7j). The similar distribution of RhoA activity and LPR was further confirmed by comparing stationary edges with contractile edges across multiple cells, averaged together (Fig. 6g). These data revealed that the nonuniform localized distribution of metabolism correlates with cytoskeleton remodelling at the subcellular level. These results further showed colocalization between LPR and RhoA activities, suggesting that an endothelial cell generates energy using glycolysis to drive actin remodelling through GTPase RhoA.

Altogether, our single-cell metabolic assays revealed molecular mechanisms through which RhoA–ROCK-1 activates SLC2A3 translocation to trigger a glycolytic burst to power the endothelial contractile apparatus across multiple endothelial types (Fig. 6h). Furthermore, subcellular analysis of LPR revealed the nonuniform, localized distribution of glycolysis at the site of actin turnover and RhoA activity, indicating that RhoA signalling coordinates energy production through glycolysis with energy consumption through cytoskeletal remodelling to control cell motility.

Discussion

Most studies measure cell metabolism using bulk assays. However, individual cells are inherently heterogeneous. Metabolic heterogeneity in endothelial cells dictates vascular activation and growth[36,37], controls cell function in infection during T-cell differentiation[38,39], affects responses to anticancer treatments within tumours[40] and results in distinct subpopulations in response to sudden changes of substrate availability among yeast cells[41], to name a few functions. Reprogrammed metabolic rates to support different cellular

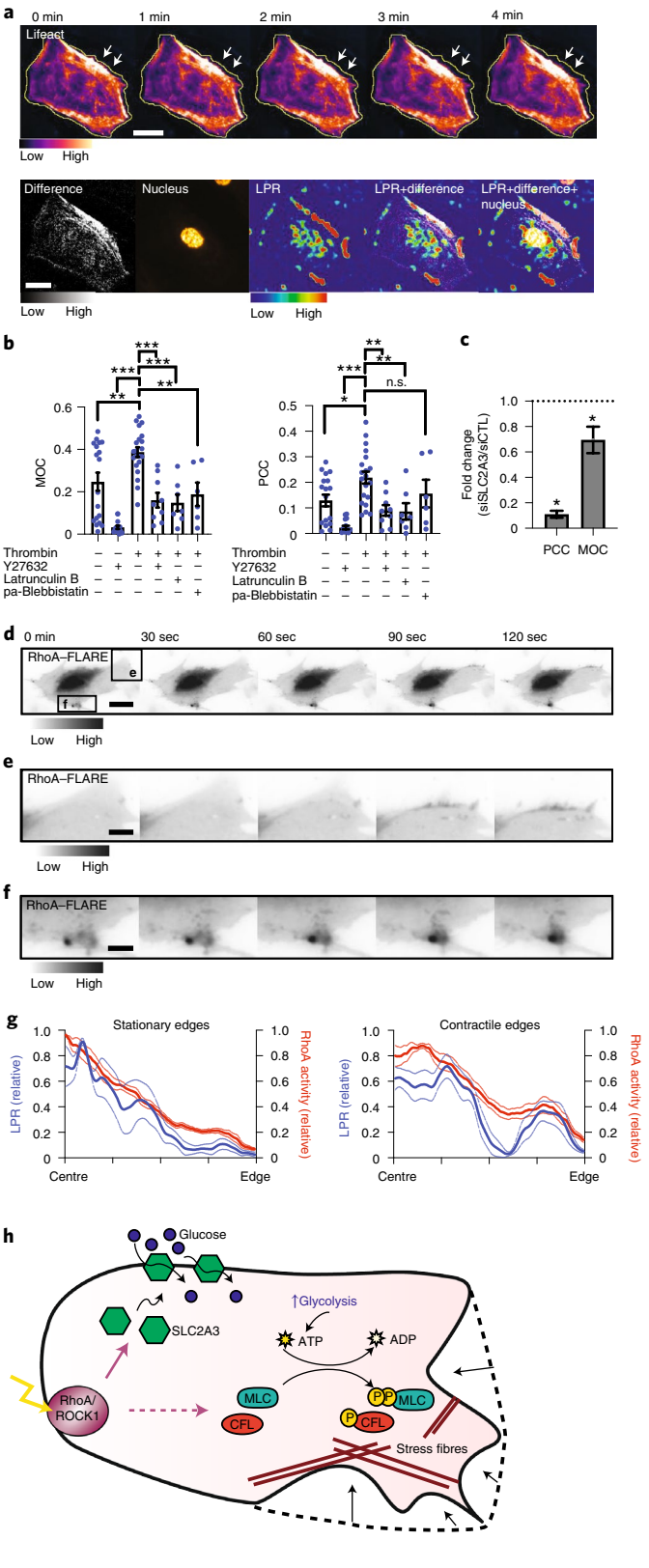

Fig. 6 | Subcellular distribution of LPR colocalizes with actin remodelling. **a**, Representative montage of endothelial cell actin structure, as labelled with Lifeact-RFP, where the yellow line indicates the original cell edge and white arrows point to the contractile edge after treatment with thrombin ($n=14$ biological replicates, 3 separate experiments). Maximum projection of change in actin structure (difference), nucleus, per-pixel LPR map (LPR) and merges. Scale bar, 30 µm. **b**, MOC and PCC of unstimulated or stimulated cells in the presence of ROCK inhibitor (Y27632), actin polymerization inhibitor (Latrunculin B) and myosin II inhibitor (para-aminoblebbistatin (paBlebbistatin)). ($n=15$, 14, 20, 9, 7, 6 from left to right; MOC thrombin versus control, $P=0.0035$; versus Y27632, $P<0.0001$; versus thrombin + Y27632, $P<0.0001$; versus thrombin + latrunculin B, $P=0.0002$; versus thrombin + para-aminoblebbistatin, $P=0.0040$; PCC thrombin versus control, $P=0.0138$; versus Y27632, $P<0.0001$; versus thrombin + Y27632, $P<0.0029$; versus thrombin + latrunculin B, $P=0.0059$; versus thrombin + para-aminoblebbistatin, $P=0.6647$). **c**, Fold change of PCC or MOC of thrombin-treated cells under SLC2A3 knockdown compared with siCTRL. ($n=14$ for both, $P=0.0317$ for PCC, $P=0.0151$ for MOC). **d**, RhoA activity measured by RhoA-FLARE in a contracting endothelial cell (scale bar ,15 µm). **e**,**f**, Regions boxed in **d** demonstrate high RhoA activity in areas of active contraction (scale bars, 4.5 µm) (**d**–**f** are representative of $n=9$ cells, 3 biological replicates). **g**, Normalized LPR (blue) and RhoA (red) activity distribution from cell centre to edge of noncontractile/stationary edges and contractile/motile edges stimulated with thrombin. (LPR stationary, $n=4$; RhoA stationary, $n=6$; LPR contract, $n=8$; RhoA contract, $n=9$). Dotted lines are s.d. **h**, Proposed mechanism of RhoA regulating glycolysis and contraction. Agonism of RhoA–ROCK-1 stimulates SLC2A3 translocation to the membrane to increase intracellular glycolysis, thereby providing the substrate for phosphorylation of downstream targets (MLC and CFL), resulting in stress-fibre formation and, ultimately, contraction. Statistical significance was determined by one-way ANOVA followed by Bonferroni test (**b**) or by two-sided Welch's *t*-test (**c**). All error bars are s.e.m.; n.s., not significant. $^{*}P \le 0.05$; $^{**}P \le 0.005$; $^{***}P \le 0.0005$.

functions have rightfully gained attention, but experimental methods to directly evaluate heterogeneous populations remain in infancy. To decipher the metabolic states of individual cells, we used a FRET-based metabolic imaging method to measure single-cell metabolism at subcellular resolution. Our single-cell metabolism method is complementary to existing ensemble metabolic assays and is broadly applicable to different cell types. With this method, we were able to investigate the underlying molecular mechanisms of glycolysis in endothelial cells. It enabled us to link heterogeneous glycolytic states to GTPase RhoA-activated phenotypes across variable time scales (low shear stress, days; migration, hours; and contraction, minutes) in individual endothelial cells. This method also allowed us to explore spatially heterogeneous metabolism and motility within individual cells. Given the feasibility, reproducibility and robustness of this approach, it should have widespread applications in studying metabolic support of single-cell functions in cell biology.

In addition to identifying single-cell metabolic heterogeneity, we found nonuniform distributions of glycolytic rates within single motile cells, specifically at sites of actin turnover and RhoA activity. RhoA-coupled glycolysis and contractile machinery, demonstrated here, also support an emerging paradigm that cellular metabolism and cytoskeleton architecture are intimately coordinated in an 'energetic metabolon'. Our results also suggest that an endothelial cell is energetically frugal and samples the environment for energetic precursors only when necessary: here, the cell employs RhoA–ROCK-1 to couple energy production with acute energy-consuming responses, such as cytoskeletal remodelling, to enable contraction. This could be functionally essential, as the continued presence of high-energy phosphates in a cell could make controlling enzymatic phosphorylation difficult. Thus, having a local, segregated pool of transmembrane receptors may enable digital-like spatial control of phosphorylation[42]. Colocalization of glycolytic enzymes with energetic demand could provide an efficient way for the cell to not only temporally determine when energy is produced, but spatially control where energy is consumed, preventing futile reactions, avoiding energy overproduction and overcoming diffusion limitation. Glycolytic metabolons have been suggested in endothelial cells, with increased ATP in the perinuclear cytosol and lamellipodial ruffles[36] and evidence that glycolytic enzymes bind to the actin cytoskeleton[43]. Here, using single-cell metabolic assays, we directly visualized the highly localized, enriched lactate production in subcellular endothelial edges and perinuclear sites, providing evidence to functionally support the glycolytic metabolon theory. Further studies linking the subcellular glycolytic rate and distribution of glycolytic machinery are needed to strengthen and validate this theory.

Integrating our single-cell metabolic method with classic molecular and functional analyses also allowed us to discover the causal role of RhoA in stimulating a SLC2A3-dependent glycolytic burst necessary for endothelial contraction. Although it is commonly recognized that SLC2A1/GLUT1 is a major glucose transporter in endothelial cells across diverse vascular beds and contributes to basal glycolysis under chronic transcriptional activation[2,26,27,44], our results revealed the critical role of SLC2A3/GLUT3 in triggering a metabolic burst, defined by a quick increase in glucose uptake, glycolysis and ATP level. ATP budget and nutrient availability play an important role in cellular decision making, including certain endothelial behaviours[17,37,45,46]. Using this mechanism, a single endothelial cell can augment its glycolytic potential even further with SLC2A3 transmembrane recruitment during acute stimuli in cellular processes requiring an immediate energy burst. We also demonstrated that vascular leak was increased in an endothelial overexpression model of SLC2A3 in vivo. In highly glycolytic platelets where SLC2A3 is enriched, thrombin (a potent platelet activator) can stimulate SLC2A3 plasma membrane translocation[47], suggesting a conserved molecular function. Exactly how RhoA–ROCK-1 causes transmembrane expression of SLC2A3 requires further exploration. Investigation of SLC2A3's role in regulating vascular pathophysiology could bolster the case that modulating signal transduction by interfering with cellular energetics could be a fruitful path to new pharmacotherapeutics in diffuse vascular pathologies[48]. The physiological role of endothelial SLC2A3 in vascular homeostasis and disease in vivo deserves future investigation.

Importantly, we found lactate production to be highest at the cell edge and centre of contractile cells. Though we attribute this to energy demand at locations of high RhoA activity, it is possible that lactate could be produced locally for usage for other cellular processes, such as histone lactylation within the nucleus[49]. Perhaps the increase of local glycolysis could act as a signal for the cell to adapt to a changing environment, thus imprinting acute stimuli into cellular memory. Future investigation of subcellular endothelial glycolysis would benefit from tracing high-energy phosphates from where they are produced to sites where they are consumed, including consideration of nuclear lactate as it corresponds to gene regulation. For instance, FRET biosensors can be further engineered with a nuclear localization sequence or plasma membrane targeting.

In summary, we investigated spatially heterogeneous endothelial motilities by developing a single-cell imaging assay to measure glycolysis at subcellular resolution. We demonstrated that endothelial migration and contraction, critical endothelial phenotypes, were driven by glycolysis at the single-cell and subcellular levels. We found energy-demanding cytoskeletal remodelling to be conducted by RhoA through SLC2A3-mediated glucose uptake and glycolysis. Altogether, our single-cell metabolic assays and mechanistic findings demonstrated the critical interplay between signalling, metabolism and motility in dictating nonuniform phenotypes of individual endothelial cells.

Methods

For additional methods, please see the Supplementary Information.

Cell culture and cloning. Human aortic endothelial cells (HAECs) (Lonza, CC-2535) were grown in endothelial growth medium (EGM2) supplemented with SingleQuots (Lonza, CC-3156 and CC-4176) and Antibiotic–Antimycotic (Gibco, 15240062) at 37 °C with 5% CO_2. HAECs were used from passages 6 to 8 for all experiments. Human pulmonary microvascular endothelial cells (HMVEC, Lonza, C12281) were maintained in EGM2-MV medium (Lonza, CC-3202) supplemented with 10% FBS. Human umbilical vein endothelial cells (HUVEC, Lonza C2519A) were maintained in EGM2-SingleQuot medium (2% FBS). HMVECs and HUVECs were used from passages 5 to 7 for all experiments. Cell lines were verified to be mycoplasma-free endothelial cells expressing CD31 by the vendor.

Laconic, LifeAct, ATeam and FLIIP-glu700 expression. Plasmids containing Laconic[8], ATeam or FLIIP-glu700 (Addgene 44238, 51958 and 17866, respectively) were cloned into Ad5 adenovirus by VectorLabs for construction of adenovirus-Laconic (ad-Lac), adenovirus-ATeam (ad-ATeam) or adenovirus-FLIIP-glu700 (ad-Glu). Ad-LifeAct-RFP (ad-LifeAct) was from Ibidi (60122). For transduction into endothelial cells, ad-Lac at 50:1 multiplicity of infection (MOI), ad-ATeam at 100:1 MOI and ad-Glu at 200:1 MOI in 1:1 EGM2 medium:Opti-MEM (Thermo Fisher, 11058021) and 3 µL GeneJammer (Agilent, 204130) per mL of final volume was added for 1 hour before replacement of medium. For migration and contraction experiments, ad-Lac and ad-LifeAct were cotransduced, each with MOI 50:1. Endothelial cells were used 48 hours post-transduction to allow for cell recovery and maximal fluorescence.

T7-eBFP2, T7-mCherry and RhoA overexpression. eBFP2 and mCherry constructs were generated from the Addgene plasmid no. 64323 and GeneCopoeia EX-C0726-M56-PFKFB3, respectively. For RhoA overexpression, pcDNA3-EGFP-RhoA-WT, pcDNA3-EGFP-RhoA-Q63L (CA), pcDNA3-EGFP-RhoA-T19N (DN) were purchased from Addgene (12965, 12968, 12967). EGFP was cloned out of each construct and replaced with either mScarlet-i (Addgene 85056 pLifeAct-mScarlet-i_N1) or eBFP2 using the vector and insert primers in Supplementary Table 1, followed by Gibson assembly (NEB, E2611). PCR products containing T7 promoters for in vitro transcription were generated using NEB Q5 polymerase (New England Biolabs, M0491) and the primers (Integrated DNA Technologies) listed in Supplementary Table 1.

Messenger RNA transcripts were generated using mMESSAGE mMACHINE T7 Ultra Kit (Thermo Fisher, AM1345). HAECs were transfected with 50 ng/cm^2

of mRNA with Lipofectamine MessengerMAX (Thermo Fisher, LMRNA003) overnight in 20% Opti-MEM–EGM2. On the day of the LPR assay, cells, each dually transfected with either mCherry and laconic or eBFP2 and laconic, were split into two groups or were mixed together into an Ibidi chamber.

RhoA–Flare expression. HAECs were plated 5×10^4 cells/well in an 8-well glass-bottom dish (Ibidi 80827) 2 days prior to the experiment. One day prior to the experiment, RhoA–Flare (Addgene, 12150) plasmid was incubated with fluorine-modified polyethylenimine (F-PEI) at a 4:1 plasmid:F-PEI mass ratio for 30 minutes in serum-free medium (Opti-MEM), then incubated with cells for 4 hours at 37 °C. The F-PEI were synthesized according to a previous method[50]. Briefly, heptafluorobutyric anhydride was added to PEI, with a molar ratio of 7:1, then trimethylamine was added at 1.5-fold mol to heptafluorobutyric anhydride. The mixture was stirred for 48 hours at room temperature, then dialysed with distilled water in a bag with a molecular-weight cut-off of 1 kDa. Medium was exchanged after the 4-hour incubation to complete endothelial growth medium (EGM2) and cells were imaged the following day.

Thrombin, lysophosphatidic acid, Y27632, latrunculin B, para-amino-blebbistatin or 2DG treatment. HAECs were first starved in EBM2 or fluorobrite medium (Gibco, A1896701) for at least 2 hours prior to thrombin treatment for 10 minutes. Thrombin was used at 0.25 U/mL for all experiments, except for that in Fig. 4d, which was 0.5 U/mL for 7–10 minutes prior to assay. Cells were treated with lysophosphatidic acid for 30 minutes prior to assay. Samples containing Y27632, latrunculin B, para-amino blebbistatin or 2DG were starved in EBM2 or Fluorobrite for 1 hour prior to thrombin treatment.

Metabolomics. Endothelial cells were plated at 500,000 cells/well using 6-well plates. Metabolites were extracted according to the manufacturer's protocol for metabolomics (HMT Metabolomics). The average lactate concentration measured by capillary electrophoresis time-of-flight mass spectrometry was 37,973.5 ± 29,376.25 pmol per million cells. Assuming an average length, height and aspect ratio of 100 µm, 4 µm and 1.12, respectively[51], the estimated lactate concentration per cell was 0.77 ± 0.82 mM.

Laconic imaging. Laconic-sensor imaging was performed on an Olympus IX-71 microscope with a ×10 objective. FRET filter sets were from Semrock: excitation 438/24, mTFP emission 483/32, Venus emission 542/27, dichroic FF458-Di02. Hoechst and TRITC filter sets for visualizing Hoechst stain, eBFP2 and mCherry were from Semrock: Hoescht excitation 337/50, Hoescht emission, 447/60, Hoescht dichroic FF409-Di03, TRITC excitation 556/20, TRITC emission 617/73, TRITC dichroic Di03-R488/561. FRET images were taken in rapid succession using a computer controlled Prior filter excitation and emission wheels and a Photometrics 95B camera. The microscope system was enclosed in a heated chamber maintained at 37 °C and 5% CO_2 for all time-lapse microscopy experiments. The microscope system was controlled by MicroManager. Imaging flow chambers (Ibidi, 80176) were used according to the manufacturer's instructions. Injections for exchanging buffers were performed manually through attached tubing.

Laconic calibration. Ad-Laconic were transduced into HAECs and were replated into Ibidi chambers at approximately 100,000 cells per chamber 24 hours later, and then were imaged 24 hours later. Cells were incubated in intracellular buffer (ICB) (10 mM NaCl, 130 mM KCl, 1.25 mM HEPES pH 7.2) with 10 µM nigericin and 2 µM rotenone with varying concentrations of sodium lactate (0.0001 mM, 0.001 mM, 0.01 mM, 0.1 mM, 1 mM and 10 mM). mTFP and Venus fluorescence channel images were acquired every 2 seconds over 3 minutes per lactate concentration. The mTFP/Venus (donor/acceptor) intensity ratio per cell after background subtraction (hereafter, 1/FRET, or FRET′ in shorthand) was obtained after segmentation (described below).

Lactate concentration and production rate (LPR) calculation. One day after ad-Lac transduction, HAECs were replated into Ibidi chambers at approximately 100,000 cells per chamber. After another 24 hours, they were starved in extracellular buffer (ECB) composed of (112 mM NaCl, 5 mM KCl, 1.25 mM $CaCl_2$, 1.25 mM $MgSO_4$, 10 mM HEPES, 24 mM $NaHCO_3$; pH 7.4) or Fluorobrite MEM (Gibco, A1896701) for at least 1 hour. The first injection was 10 mM glucose in ECB, then after 3 minutes, 10 mM glucose and 500 µM pCMBA in ECB. The fluorescence images of mTFP and Venus were obtained with exposures between 100–300 ms/frame every 2 seconds until completion of the assay. LPRs were calculated as follows: after pCMBA injection, the FRET′ rose ($\Delta FRET^{-1}$) as cells accumulated intracellular lactate. From the FRET′ versus lactate calibration curve, we define c as a constant in eq. 1 which we use in eq. 2 to finally define LPR in eq. 3.

$$\frac{\Delta FRET^{-1}}{\Delta log_{10} lactate} = c \quad (1)$$

$$\frac{\Delta FRET^{-1}}{\Delta t} = c\frac{\Delta log_{10} lactate}{\Delta t}. \quad (2)$$

$$LPR = \frac{\Delta log_{10} lactate}{\Delta t}. \quad (3)$$

Intracellular lactate was determined by first estimating the FRET′ signal at zero lactate, which was after starvation for 1 hour in extracellular buffer and perfusion with 10 mM pyruvate. Following 10 mM glucose perfusion, the FRET′ signal reached steady state after 2 minutes. At the end of each experiment, the FRET′ value at 10 mM lactate was measured such that each cell had its own two-point calibration curve. An average FRET′ value over 20 seconds during steady state was used to determine intracellular lactate.

DMOG stimulation of endothelial cells. HAECs were plated to confluency and transduced with ad-Lac at 50 MOI 2 days prior to the LPR assay. One day prior to the LPR assay, cells were transfected with either T7-eBFP2 or T7-mCherry at 50 ng/cm^2. The night before the assay, the cells were treated with 0.5 mM of DMOG or DMSO in EGM2. On the day of the LPR assay, cells, each dually labelled with either mCherry and laconic or eBFP2 and laconic, were split into two groups or were mixed together into an Ibidi chamber.

RhoA-Q63L or RhoA-T19N expression in endothelial cells. HAECs were plated to confluency and transduced with ad-Lac at 50 MOI two days prior to the LPR assay. One day prior to the LPR assay, cells were transfected with either T7-eBFP2-RhoA-Q63L, T7-mScarlet-i-RhoA-T19N, T7-eBFP2-RhoA-T19N or T7-mScarlet-i-RhoA-Q63L at 25 ng/cm^2. On the day of the LPR assay, cells, each dually labelled with either mScarlet-i and laconic or eBFP2 and laconic, were split into two groups or mixed together into an Ibidi chamber.

siRNA expression in endothelial cells with LPR measurements. Two days prior to the LPR assay, HAECs plated to confluency were transduced with ad-Lac at 50 MOI, ad-ATeam at 100 MOI, or ad-FLIIP-Glu700 at 200 MOI. Twelve hours later, the cells were transfected with either scrambled control or siRNA targeted towards *SLC2A3*, as above.

Deep-learning-enabled segmentation of cells. *Sample generation for ground truth.* Endothelial cells were transduced with ad-Lac at 50 MOI, as above. After 48 hours of transduction, cells were fixed for immunofluorescence as described above for VE-Cadh (CDH5) to mark cell boundaries and were stained with Hoechst (1:1,000). Samples were then stored at 4 °C wrapped in parafilm to be imaged at a later time. Images of cells were acquired in the FRET channel and Hoechst channel at ×10 magnification.

Ground-truth labelling. Cellprofiler[52] was used for ground-truth labelling of four classes: background, border, cytoplasm and nuclei. First, 1200×1200-pixel images in the FRET channel were background corrected with subtraction using a running average block size of 150 pixels across all images of the fixed samples. Next, using an adaptive threshold (Otsu) strategy, nuclei were identified after staining with Hoechst dye. With nuclei as seeds, cell boundaries were found through the propagation algorithm. The cytoplasm was then defined as areas inside the cell boundaries (through immunofluorescence labelling with anti-CDH5 and secondary antibody anti-rabbit-Alexa 488), but not of the nuclei. Next, these images were recombined and labelled with a unique class identifier. Minor adjustments to the labelled images were made algorithmically and automatically in MATLAB, including making sure that a cell boundary encapsulated all cytoplasm and nuclei, and getting rid of cells that had no nuclei. Images of each label class were generated and visually inspected for accuracy; 432 images containing approximately 500 cells per image were used for training, as described below. Of note, ground-truth labelling required separate nuclei- and boundary-staining procedures, which would have to be repeated on each separate dataset for precise determination of cell boundaries. This makes fast determination of LPR without manual boundary tracing impractical (we routinely collect hundreds of cells in each experiment). With deep learning, it became possible to avoid the two extra staining procedures and thereby increase experimental throughput, and has the added benefit of being generalizable to other cell types and magnifications.

Deep-learning-enabled semantic segmentation. The 432-image data set with labelled ground truth was randomized into training (70%), validation (15%) and test (15%) datasets. To enhance the dataset, patches were extracted and augmented with random reflection, rotation and shear up to 10 degrees. Next, a U-net network[7] (Extended Data Fig. 1b) was trained using conventional deep learning, with final layer pixel classification consisting of an inverse class weighting (based on class frequency) cross entropy loss function over 50 epochs. A 128×128-pixel image tile size was chosen, with 8 minibatches, using stochastic gradient of descent with 0.95 momentum (~38,000 unique images prior to augmentation; background pixels, 2.93×10^8; border pixels, 2.81×10^7; cell-body pixels, 9.15×10^7; nuclei pixels, 2.54×10^7). The initial learning rate was 0.001 and was dropped by a factor

of 10 every 10 epochs. The training was performed in MATLAB using the Deep Learning Toolbox on 2 NVIDIA GeForce 1080 Ti and 1 NVIDIA Titan V GPU. Total training time was about 96 hours and was stopped after no further reduction of loss. In this manner, a semantic segmentation network capable of assigning each pixel a separate class was created. Measures of deep-learning accuracy are listed in Table 1. We found that inclusion of a nuclei class improved the classification of cell boundaries. Adding additional 2D convolutional layers to increase the receptive field did not improve the network accuracy but reduced the learning rate. Convolutional layers had a 3 × 3 kernel size. Skip connections were included in the U-net as depicted, in Extended Data Fig. 1b.

Image analysis. After feeding images into the semantic segmentation network, the output was further processed to remove cells below a predefined threshold, based on expected cell size. Next, FRET′ trajectories of each cell over time were generated. To accomplish this, individual cells were extracted from the labelled images: each cell was identified as an object surrounded by a boundary class and containing a nucleus. The mean position of the cell was matched to a cell with the closest position in a subsequent image, thus generating a position trajectory, and therefore FRET′ trajectory (computed as the average mTFP fluorescence intensity divided by the average Venus fluorescence intensity inside the boundary minus background signal) of every cell. The FRET′ trajectories were then subjected to a median filter of width 5 for denoising. To obtain the LPR, pyruvate-production rate or glucose-uptake rate, the slope of the FRET′ (or regular FRET for glucose sensor) signal was calculated over 40-second trajectories and fit against a linear model during the portion of the time the cells were exposed to MCT1 inhibitor. ATP levels were determined by the average FRET signal before and after addition of agonist. Only if the R^2 value of the fit was greater than 0.9 was the data considered useable. Conversion of FRET′ to LPR was calculated as described above.

Quantification of image analysis error. We estimated the error in deep-learning-assisted semantic segmentation by first computing the error between ground-truth fluorescence and segmented fluorescence. First, we used a test data set of cells expressing laconic, for which we have ground truth, and segmented these images with the deep-learning algorithm. Then, using the same image analysis pipeline, we plotted the cell fluorescence as estimated from deep learning networks against the ground-truth cell fluorescence (n = ~20,000). The 95% confidence interval of the slope was 0.93–0.95, so there was consistently a small underestimation of the true fluorescence of each cell (Extended Data Fig. 1c).

To estimate how this error in fluorescence detection affects fitting of LPR data, we turned to Monte Carlo simulations of LPR (bootstrapping). Using the dataset (Extended Data Fig. 1c), which provides a real measure between ground truth and fluorescence, we generated a line $x=y$ by randomly sampling the ground-truth fluorescence, each of which corresponds to a deep-learning generated fluorescence, 100 times. The slope of this line was then calculated by performing linear regression. This random sampling of fluorescence values, followed by slope calculation, simulates LPR calculation in real samples. The distribution of these bootstrapped slopes was plotted after this was repeated 10,000 times, resulting in a Gaussian distribution of slopes (Extended Data Fig. 1d). The red line is fit to a Gaussian. The mean of the fit Gaussian is 0.9, similar to the correlation between ground truth and deep-learning fluorescence above (0.94). The s.d. of the Gaussian fit is 0.05. Thus the error in estimating LPR, due to semantic segmentation, is 0.05/0.9 which is approximately 5%.

Per-pixel LPR. Cells were seeded into Ibidi chambers and the same protocol followed when imaging LPR as above, with the exception that a ×40 plan-apochromat Olympus objective was used for imaging. After acquisition of the images, a tophat filter with width of 30 µm (in real space) was used to estimate the background. A Gaussian with width of 1 pixel was convolved with the original image to smooth noise artefact. To this smoothened image, the minimum of the estimated background image was subtracted. FRET′ was calculated by dividing the mTFP image from the YFP image. Then, the per-pixel LPR was calculated after binning by 4 in an average sense (super pixel) in each image in the time series (after addition of pCMBA). The slope of each super pixel in the time series was then calculated; the value of the slope was replotted as the LPR image. LPR images were then resized to the original size.

Actin turnover and overlap calculations. Ten Lifeact–RFP images, taken 1 minute apart, were subtracted from each other in sequential order, and the maximum intensity of each of these difference images was projected as the final 'difference' image. Both the Lifeact difference image and LPR images were normalized to the largest value in the respective image. To calculate the Manders' Overlap Coefficient (MOC) or Pearson's Correlation Coefficient (PCC) (complementary statistical measures of spatial correlation) between the Lifeact difference image and the per-pixel LPR image, Lifeact difference images were first segmented by hand. The mask of the cell was then applied to the LPR per-pixel image to avoid background effects. Next, the actin difference image was thresholded at 5% maximum intensity. Finally, the MOC and PCC were calculated as in eq. 4 and eq. 5, respectively.

$$MOC = \frac{\sum_{i,j} x_{i,j} \cdot y_{i,j}}{\sum_{i,j} x_{i,j} \sum_{i,j} y_{i,j}} \quad (4)$$

$$PCC = \frac{\sum_{i,j} \left(x_{i,j} - x_{i,j}\right) \cdot \left(y_{i,j} - y_{i,j}\right)}{\sum_{i,j} \left(x_{i,j} - x_{i,j}\right) \sum_{i,j} \left(y_{i,j} - y_{i,j}\right)} \quad (5)$$

where x and y are Lifeact difference and LPR images with i rows and j columns, and $\langle \bullet\bullet\bullet \rangle$ operator denotes the mean. Simulated MOC or PCC was performed by randomizing the spatial location of the LPR pixel values within the masked area and calculating the MOC or PCC with the thresholded Lifeact difference image 10,000 times.

RhoA imaging, LPR versus RhoA activity. RhoA–Flare imaging was performed with FRET filter sets purchased from Semrock: excitation 438/24, mTFP emission 483/32, Venus emission 542/27 and dichroic FF458-Di02 on transfected cells. Integration times ranged from 100 ms to 500 ms with a Photometrics Prime95b camera using either a ×40 or ×100 plan-apochromat Olympus objective. Single-cell LPR was performed on separate cells as described above. To calculate the LPR or RhoA activity as a function of distance from centre, the cells were first segmented by hand in ImageJ. Line scan intensities of either RhoA activity (FRET) or LPR were performed from the geometric centre of the cell to the edge of the contracting or non-contracting portions of the cell. These line scans were then normalized to maximum intensity and interpolated using cubic splines to the same number of data points (1,000). The signals were then averaged to produce the final figure. Each line scan in the category of contractile or not is from a different cell.

Mouse studies. Gene Expression Omnibus datasets (GEOD) were downloaded from EndoDB (https://endotheliomics.shinyapps.io/endodb/), a database of curated endothelial transcriptomics datasets[31]. All mouse endothelial datasets are of isolated primary cells in the untreated (control) arms of the experiments.

All animal care and treatment procedures were approved by the University of Chicago Institutional Animal Care and Use Committee. Animals were handled according to the National Institutes of Health Guide for the Care and Use of Laboratory Animals and all experiments were compliant with ethical guidelines from The Guide for the Care and Use of Laboratory Animals. All experimental animals were assigned unique identifiers to blind experimenter to treatment. For the mouse model of vascular leak, C57BL/6J mice were purchased from Jackson Laboratories. All experimental animals were maintained in a pathogen-free environment with a humidity of 40–60%, a temperature of 20–24 °C and a 12-hour light/dark cycle at the University of Chicago. For in vivo human *SLC2A3* or mScarlet-i transient overexpression, C57BL/6 mice, 10–12 weeks old, were tail-vein-injected with the solution containing 40 µg of endotoxin-free *CDH5-SLC2A3* overexpression plasmid, *CDH5*-mScarlet-i or control CDH5-containing plasmid DNA diluted with sterile 5% glucose and then mixed with polyethylenimine (PEI) nanoparticles (TurboFect in vivo Transfection Reagent) (Thermo Scientific), according to the manual's instructions. After 24 hours, mice were anaesthetized with ketamine–xylazine (80 mg/kg:20 mg/kg) before collection of aorta and intimal RNA isolation, Evans blue assay or fixation, paraffin-embedding and sectioning for visualization of mScarlet-i.

Evans blue dye assay. After anaesthesia, retro-orbital injection of 4 µL/g of 2% Evans blue dye was performed. One hour later, aortas were immediately cleaned and collected, photographed and weighed. Evans blue dye was extracted from the aortas by sonication in 50% trichloroacetic acid (4 µL/mg). Each sample was centrifuged, and the supernatant mixed with 100% ethanol in a 1:3 ratio. The OD of each sample was read at 620 nm on a Biotek-3 instrument and normalized to aorta weight.

Aorta intima isolation for qRT–PCR. After careful isolation, the aorta was quickly flushed with 350 µL of QIAzol lysis reagent (Qiagen) using a 29-G insulin syringe, and the elute was collected in a microfuge tube for intimal RNA isolation. The leftover aorta after flushing with QIAzol was homogenized with 700 µL of QIAzol for RNA isolation of medium and adventitia. Reverse transcription and qRT–PCR were performed using the Maxima First Strand cDNA Synthesis Kit (Thermo Fisher), according to the manufacturer's protocol. Mouse PCR primers are provided in Supplementary Table 2.

Fluorescence of aortic intima. CDH5-mScarlet-i transfected aortas were fixed in 4% paraformaldehyde for 15 minutes and embedded in OCT after being immersed in OCT:sucrose (1:1) mixed solution for 24 hours. Frozen samples were sectioned 5–8 µm. The sections were then mounted, permeabilized, blocked and incubated with antibody to CDH5, followed by fluorescent secondary antibody (as above). Samples were then incubated with ProLong Gold with DAPI (Thermo Fisher) and imaged with a confocal microscope (Olympus).

Statistics. The data were analysed in Prism 9 (GraphPad Software). All data with error bars are shown as mean ± s.e.m. except for the metabolomics estimate which is mean ± s.d. (Fig. 1) to better highlight the distribution of intracellular

lactate levels. Statistical significance was determined by unpaired Welch's *t*-test for individual differences and one-way ANOVA, followed by Bonferroni's test for multiple comparisons. All *t*-tests were two-tailed. All experiments were biological replicates, except for extracellular flux experiments, which included technical replicates. All measurements were taken from distinct samples.

Reporting Summary. Further information on research design is available in the Nature Research Reporting Summary linked to this article.

Data availability

Gene Expression Omnibus datasets (GEOD) were downloaded from EndoDB (https://endotheliomics.shinyapps.io/endodb/): E-GEOD-15760, E-GEOD-20741, E-MTAB-5921, E-GEOD-40999, E-GEOD-16067, E-GEOD-11870, E-GEOD-1576, E-GEOD-47067. Original data that support our findings in this study are available from the corresponding author upon reasonable request or at https://doi.org/10.5281/zenodo.4638059. Source data are provided with this paper.

Code availability

The code generated during this study is available at https://github.com/wulab-code/laconic without restriction.

Received: 31 March 2020; Accepted: 12 April 2021;
Published online: 24 May 2021

References

1. Kim, B., Li, J., Jang, C. & Arany, Z. Glutamine fuels proliferation but not migration of endothelial cells. *EMBO J.* **36**, 2321–2333 (2017).
2. Wu, D. et al. HIF-1α is required for disturbed flow-induced metabolic reprogramming in human and porcine vascular endothelium. *eLife* **6**, e25217 (2017).
3. Feng, S. et al. Mechanical activation of hypoxia-inducible factor 1α drives endothelial dysfunction at atheroprone sites. *Arterioscler Thromb. Vasc. Biol.* **37**, 2087–2101 (2017).
4. Doddaballapur, A. et al. Laminar shear stress inhibits endothelial cell metabolism via KLF2-mediated repression of PFKFB3. *Arterioscler Thromb. Vasc. Biol.* **35**, 137–145 (2015).
5. van Nieuw Amerongen, G. P., Koolwijk, P., Versteilen, A. & van Hinsbergh, V. W. Involvement of RhoA/Rho kinase signaling in VEGF-induced endothelial cell migration and angiogenesis in vitro. *Arterioscler Thromb. Vasc. Biol.* **23**, 211–217 (2003).
6. Van Valen, D. A. et al. Deep learning automates the quantitative analysis of individual cells in live-cell imaging experiments. *PLoS Comput. Biol.* **12**, e1005177 (2016).
7. Ronneberger, O., Fischer, P. & Brox, T. U-Net: convolutional networks for biomedical image segmentation. in *Medical Image Computing and Computer-Assisted Intervention – MICCAI 2015*. 234–241 (2015).
8. San Martin, A. et al. A genetically encoded FRET lactate sensor and its use to detect the Warburg effect in single cancer cells. *PLoS ONE* **8**, e57712 (2013).
9. Csurka, G., Larlus, D. & Perronnin, F. What is a good evaluation measure for semantic segmentation? In *Proc. British Machine Vision Conference* (BMVA Press, 2013).
10. Halestrap, A. P. Monocarboxylic acid transport. *Compr. Physiol.* **3**, 1611–1643 (2013).
11. Sonveaux, P. et al. Targeting the lactate transporter MCT1 in endothelial cells inhibits lactate-induced HIF-1 activation and tumor angiogenesis. *PLoS ONE* **7**, e33418 (2012).
12. San Martin, A. et al. Imaging mitochondrial flux in single cells with a FRET sensor for pyruvate. *PLoS ONE* **9**, e85780 (2014).
13. Takanaga, H., Chaudhuri, B. & Frommer, W. B. GLUT1 and GLUT9 as major contributors to glucose influx in HepG2 cells identified by a high sensitivity intramolecular FRET glucose sensor. *Biochim. Biophys. Acta* **1778**, 1091–1099 (2008).
14. Imamura, H. et al. Visualization of ATP levels inside single living cells with fluorescence resonance energy transfer-based genetically encoded indicators. *Proc. Natl Acad. Sci. USA* **106**, 15651–15656 (2009).
15. Davies, P. F. Flow-mediated endothelial mechanotransduction. *Physiol. Rev.* **75**, 519–560 (1995).
16. Mayor, R. & Etienne-Manneville, S. The front and rear of collective cell migration. *Nat. Rev. Mol. Cell Biol.* **17**, 97–109 (2016).
17. Diebold, L. P. et al. Mitochondrial complex III is necessary for endothelial cell proliferation during angiogenesis. *Nat. Metab.* **1**, 158–171 (2019).
18. Mole, D. R. et al. 2-Oxoglutarate analogue inhibitors of hif prolyl hydroxylase. *Bioorg. Medicinal Chem. Lett.* **13**, 2677–2680 (2003).
19. Fazal, F. et al. Essential role of cofilin-1 in regulating thrombin-induced RelA/p65 nuclear translocation and intercellular adhesion molecule 1 (ICAM-1) expression in endothelial cells. *J. Biol. Chem.* **284**, 21047–21056 (2009).
20. van Nieuw Amerongen, G. P., Vermeer, M. A. & van Hinsbergh, V. W. Role of RhoA and Rho kinase in lysophosphatidic acid-induced endothelial barrier dysfunction. *Arterioscler Thromb. Vasc. Biol.* **20**, E127–E133 (2000).
21. van Nieuw Amerongen, G. P., van Delft, S., Vermeer, M. A., Collard, J. G. & van Hinsbergh, V. W. Activation of RhoA by thrombin in endothelial hyperpermeability: role of Rho kinase and protein tyrosine kinases. *Circ. Res.* **87**, 335–340 (2000).
22. Blanchoin, L., Boujemaa-Paterski, R., Sykes, C. & Plastino, J. Actin dynamics, architecture, and mechanics in cell motility. *Physiol. Rev.* **94**, 235–263 (2014).
23. Goddard, L. M. & Iruela-Arispe, M. L. Cellular and molecular regulation of vascular permeability. *Thromb. Haemost.* **109**, 407–415 (2013).
24. Mehta, D. & Malik, A. B. Signaling mechanisms regulating endothelial permeability. *Physiol. Rev.* **86**, 279–367 (2006).
25. Vandenbroucke, E., Mehta, D., Minshall, R. & Malik, A. B. Regulation of endothelial junctional permeability. *Ann. N. Y. Acad. Sci.* **1123**, 134–145 (2008).
26. Tang, M. et al. Brain microvasculature defects and Glut1 deficiency syndrome averted by early repletion of the glucose transporter-1 protein. *Nat. Commun.* **8**, 14152 (2017).
27. Fessel, J. P. et al. Metabolomic analysis of bone morphogenetic protein receptor type 2 mutations in human pulmonary endothelium reveals widespread metabolic reprogramming. *Pulm. Circ.* **2**, 201–213 (2012).
28. Sasmal, D. K. et al. TCR–pMHC bond conformation controls TCR ligand discrimination. *Cell Mol. Immunol.* **17**, 203–217 (2020).
29. Sasmal, D. K., Pulido, L. E., Kasal, S. & Huang, J. Single-molecule fluorescence resonance energy transfer in molecular biology. *Nanoscale* **8**, 19928–19944 (2016).
30. Fraccaroli, A. et al. Endothelial α-parvin controls integrity of developing vasculature and is required for maintenance of cell-cell junctions. *Circ. Res.* **117**, 29–40 (2015).
31. Khan, S. et al. EndoDB: a database of endothelial cell transcriptomics data. *Nucleic Acids Res.* **47**, D736–D744 (2019).
32. Wu, C. et al. Mechanosensitive PPAP2B regulates endothelial responses to atherorelevant hemodynamic forces. *Circ. Res.* **117**, e41–e53 (2015).
33. Yao, L., Xue, X., Yu, P., Ni, Y. & Chen, F. Evans blue dye: a revisit of its applications in biomedicine. *Contrast Media Mol. Imaging* **2018**, 7628037 (2018).
34. Riedl, J. et al. Lifeact: a versatile marker to visualize F-actin. *Nat. Methods* **5**, 605–607 (2008).
35. Pertz, O., Hodgson, L., Klemke, R. L. & Hahn, K. M. Spatiotemporal dynamics of RhoA activity in migrating cells. *Nature* **440**, 1069–1072 (2006).
36. De Bock, K. et al. Role of PFKFB3-driven glycolysis in vessel sprouting. *Cell* **154**, 651–663 (2013).
37. Wilhelm, K. et al. FOXO1 couples metabolic activity and growth state in the vascular endothelium. *Nature* **529**, 216–220 (2016).
38. Karmaus, P. W. F. et al. Metabolic heterogeneity underlies reciprocal fates of T_H17 cell stemness and plasticity. *Nature* **565**, 101–105 (2019).
39. Bantug, G. R., Galluzzi, L., Kroemer, G. & Hess, C. The spectrum of T cell metabolism in health and disease. *Nat. Rev. Immunol.* **18**, 19–34 (2018).
40. Hensley, ChristopherT. et al. Metabolic heterogeneity in human lung tumors. *Cell* **164**, 681–694 (2016).
41. van Heerden, J. H. et al. Lost in transition: start-up of glycolysis yields subpopulations of nongrowing cells. *Science* **343**, 1245114 (2014).
42. Huang, J. et al. A single peptide-major histocompatibility complex ligand triggers digital cytokine secretion in $CD4^+$ T cells. *Immunity* **39**, 846–857 (2013).
43. Masters, C. Interactions between glycolytic enzymes and components of the cytomatrix. *J. Cell Biol.* **99**, 222s–225s (1984).
44. Huang, Y. et al. Normal glucose uptake in the brain and heart requires an endothelial cell-specific HIF-1α-dependent function. *Proc. Natl Acad. Sci. USA* **109**, 17478–17483 (2012).
45. Kuo, A., Lee, M. Y. & Sessa, W. C. Lipid droplet biogenesis and function in the endothelium. *Circ. Res.* **120**, 1289–1297 (2017).
46. Yu, P. et al. FGF-dependent metabolic control of vascular development. *Nature* **545**, 224–228 (2017).
47. Sorbara, L. R. et al. Thrombin-induced translocation of GLUT3 glucose transporters in human platelets. *Biochem. J.* **328**, 511–516 (1997).
48. Huang, R. T. et al. Experimental lung injury reduces Kruppel-like factor 2 to increase endothelial permeability via regulation of RAPGEF3–Rac1 signaling. *Am. J. Respir. Crit. Care Med* **195**, 639–651 (2017).
49. Zhang, D. et al. Metabolic regulation of gene expression by histone lactylation. *Nature* **574**, 575–580 (2019).
50. Li, L. et al. Artificial virus delivers CRISPR–Cas9 system for genome editing of cells in mice. *ACS Nano* **11**, 95–111 (2017).
51. Barbee, K. A., Davies, P. F. & Lal, R. Shear stress-induced reorganization of the surface topography of living endothelial cells imaged by atomic force microscopy. *Circ. Res.* **74**, 163–171 (1994).

52. Carpenter, A. E. et al. CellProfiler: image analysis software for identifying and quantifying cell phenotypes. *Genome Biol.* **7**, R100 (2006).

Acknowledgements
This work was supported by NIH grants R00AI106941 (J.H.), R21AI120010 (J.H.), R01HL138223 (Y.F.) and R01HL136765 (Y.F.), NIH New Innovator Award DP2AI144245 (J.H.), T32EB009412 (D.L.H.), T32HL007381 (D.L.H.) and F32HL134288 (D.W.) and NIH Pathway to Independence Award K99HL145113 (D.W.) and R00HL145113 (D.W.). NVIDIA GPU Grant (D.W.), CSCTR Early Career Development Award (D.W.) and NSF Career Award 1653782 (J.H.) also supported this work.

Author contributions
D.W. and D.L.H. planned and executed experiments, analysed data and interpreted results. T.S. analysed data. C.-F.Y., A.M., T.-P.S., R.-T.H. and Z.Z. performed experiments. J.H. and Y.F. planned experiments and interpreted results. G.M.M. helped to design experiments. D.W., D.L.H., J.H. and Y.H. wrote and edited the manuscript.

Competing interests
The authors declare no competing interests.

Additional information
Extended data is available for this paper at https://doi.org/10.1038/s42255-021-00390-y.

Supplementary information The online version contains supplementary material available at https://doi.org/10.1038/s42255-021-00390-y.

Correspondence and requests for materials should be addressed to J.H. or Y.F.

Peer review information *Nature Metabolism* thanks Ali Ertürk, Marc Tramier and the other, anonymous, reviewer(s) for their contribution to the peer review of this work. Primary Handling Editor: Christoph Schmitt.

Reprints and permissions information is available at www.nature.com/reprints.

Publisher's note Springer Nature remains neutral with regard to jurisdictional claims in published maps and institutional affiliations.

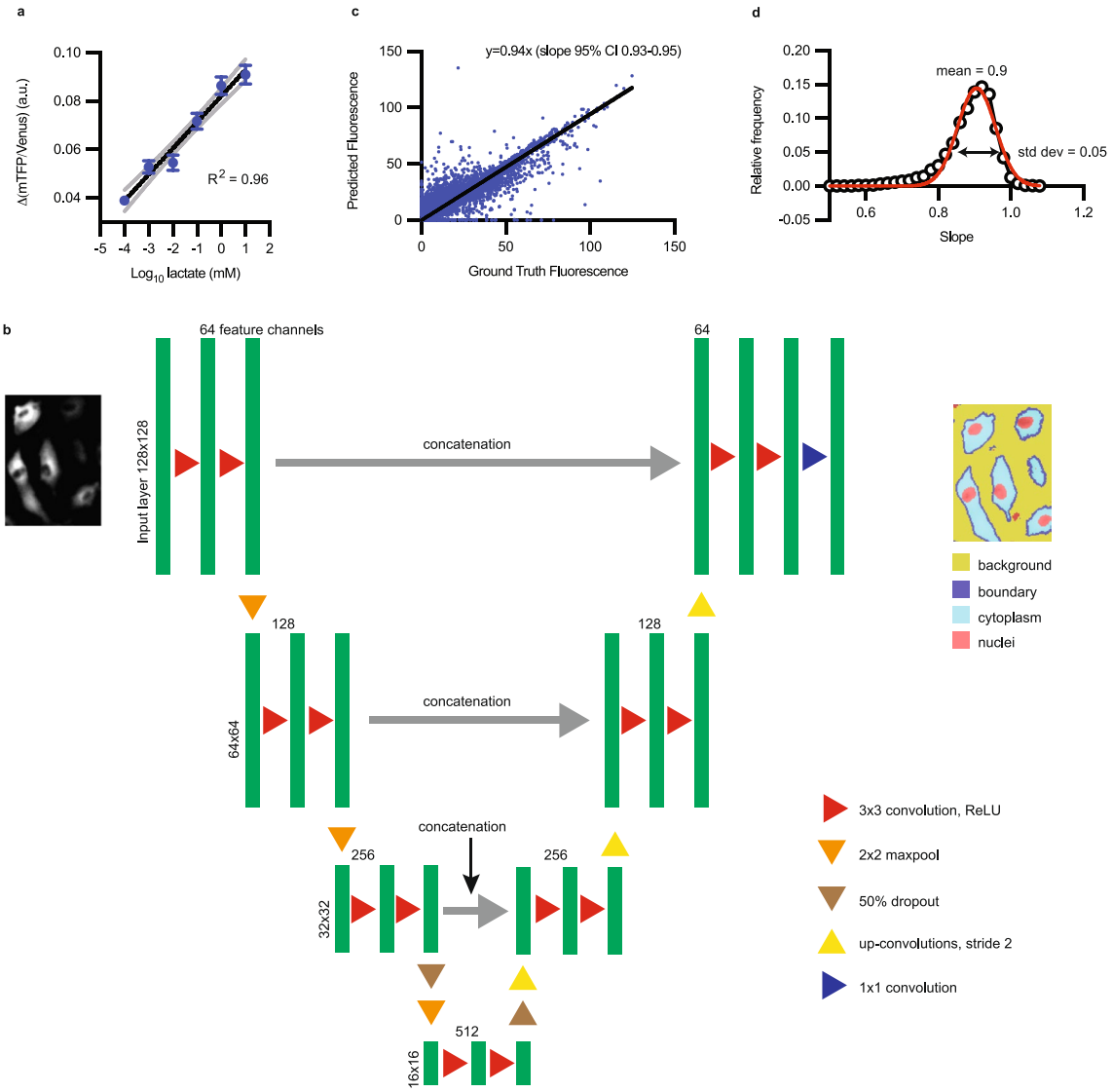

Extended Data Fig. 1 | Single-cell metabolic assay utilizes deep learning-enabled segmentation. a, mTFP/Venus (or 1/FRET) change is linearly correlated over 6 orders of magnitude of log lactate (n = 287 cells; black line is semilog fit with $R^2 = 0.96$, gray dotted lines are 95% confidence interval); error bars are SEM. Standard deviation of regression coefficients for R^2 for (**a**) is 0.049. **b**, Deep learning architecture for semantic segmentation, modified from Ronneberger et al[7]. The U-Net consisted of a contracting path (encoder) and an expansive path (decoder). The contracting path consists of layers composed of two 3 × 3 convolutions, each followed by a rectified linear unit (ReLU) activation function. Each layer is followed by a 2 × 2 max pooling operation with a stride of two- which will double the number of feature channels being used. The convolutions start with 64 feature channels and 128 × 128 images and continue until they reach 512 channels and 16 × 16 images. In the expansive path, 2 × 2 up-convolutions (up sampling) of stride 2 to decrease by half the feature channels and increase the size of the image. The layers composed of 3 × 3 convolutions and ReLU are concatenated with the pair of layers in the contracting side, in order to reinclude the localization information. In the final layer, a 1 × 1 convolution layer is used to map the resulting 64-component feature channels vector to the 4 segmentation channels for background, boundary, cytoplasm, and nuclei. **c**, Ground Truth Fluorescence vs. Predicted Fluorescence, as evaluated with deep-learning-enabled semantic segmentation. (n ~ 20,000 cells) Ground truth fluorescence was defined as signal inside the cell boundary. C.I., confidence interval. **d**, Frequency distribution of fluorescence slopes. Data from (**c**) were randomly sampled 100 times and fitted to a line. This process was repeated 10,000 times and the distribution of fitted slopes was plotted (open black circles). The red line is a Gaussian fit with mean 0.9 and standard deviation of 0.05. Thus, the error in estimating slopes of fluorescence is approximately 0.05/0.9, or approximately 5%.

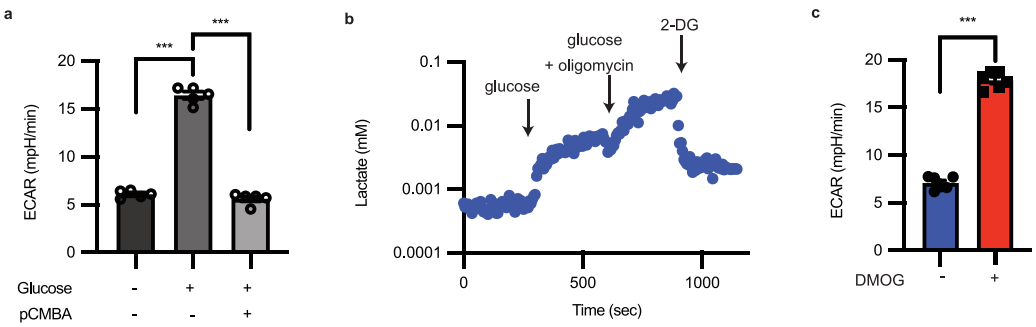

Extended Data Fig. 2 | Single-cell laconic accurately mimics bioenergetics assays. a, Extracellular flux assay of HAECs treated with glucose then pCMBA (n = 5) using Seahorse; biological replicates, error bars are s.e.m., $P < 0.0001$ for both comparisons. **b**, A single-cell glycolytic stress test using lactate FRET sensor. Cells were first starved in zero glucose buffer for 1 hour. Glucose addition increased intracellular lactate, which was further increased by adding oligomycin and glucose. Addition of 2-deoxyglucose (2-DG) blocked all glycolysis, causing intracellular lactate to drop. **c**, Overnight treatment of endothelial cells with 500 μM DMOG increases ECAR measured by extracellular flux relative to DMSO-treated cells using Seahorse. (n = 11 combined biological and technical replicates for each condition; error bars are s.e.m., $P < 0.0001$). Statistical significance determined by one-way ANOVA followed by Bonferroni test (**a**) or by two-sided Welch's t-test (**c**). ***$P <= 0.0005$.

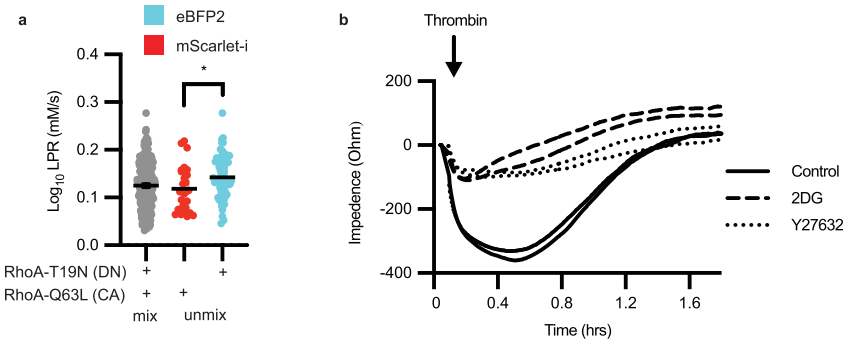

Extended Data Fig. 3 | RhoA activity induces contraction using glycolysis. a, LPR of HAECs transfected with either RhoA-T19N-eBFP2 (dominant negative (DN) form, cyan) or RhoA-Q63L-mScarlet-i (constitutively active (CA) form, red), mixed, then deconvoluted by colour (n = 174 "cyan" and 52 "red", respectively). Error bars are s.e.m., $P = 0.0193$. **b**, TEER measurement of HAECs after thrombin treatment, either pre-treated with Y27632 or 2DG compared to control (no Y27632 or 2DG). Statistical significance determined by two-sided Welch's t-test. *P <= 0.05.

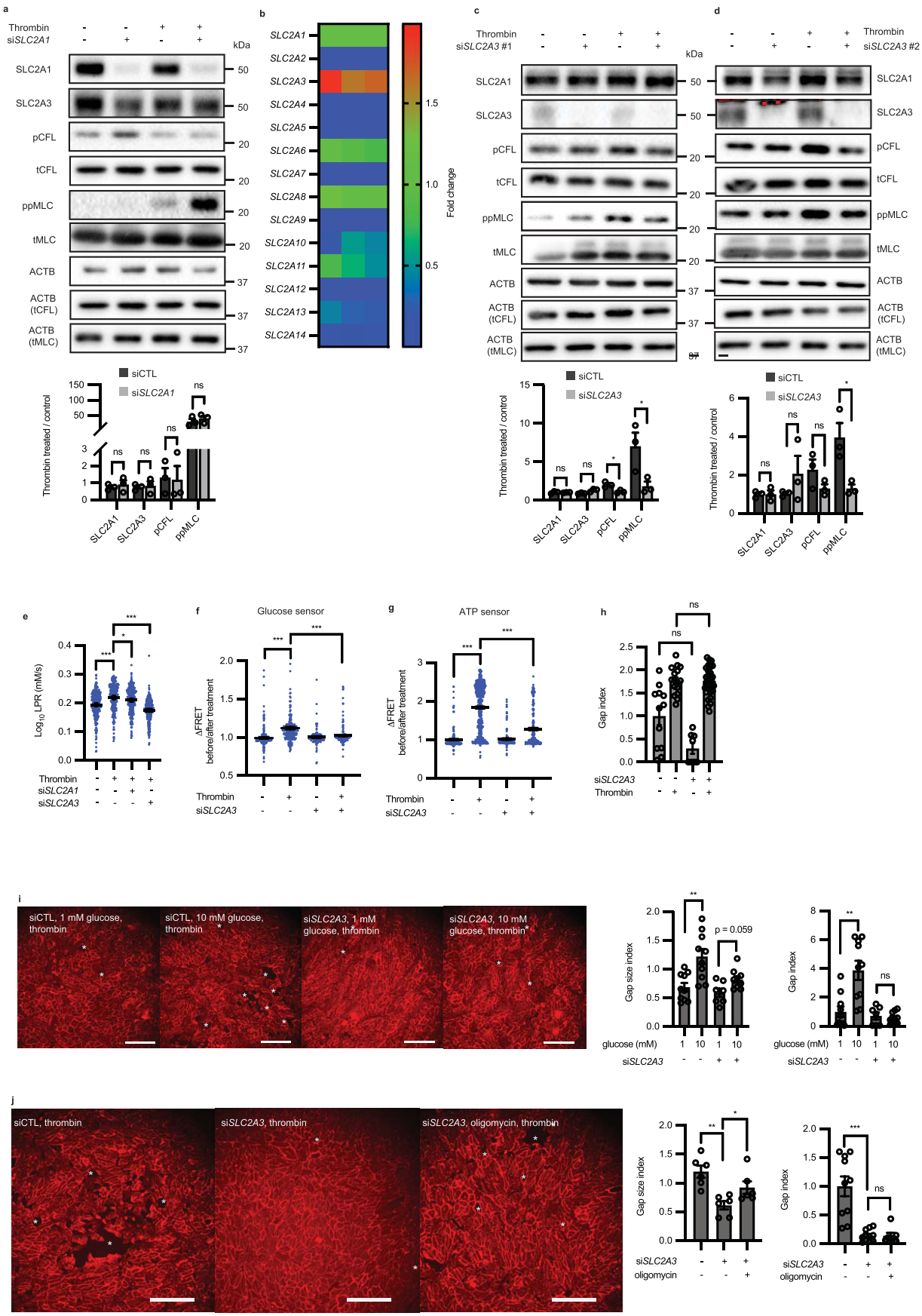

Extended Data Fig. 4 | See next page for caption.

Extended Data Fig. 4 | SLC2A3 but not SLC2A1 knockdown mitigates thrombin-induced phosphorylation of CFL and MLC and glycolysis. a, Western blot of SLC2A1, SLC2A3, phospho-cofilin and phospho-MLC in the presence or absence of siRNA targeted towards *SLC2A1* and thrombin treatment (n = 3 biological replicates). Loading control for each protein is ACTB unless specifically denoted in parentheticals. Phospho-proteins are additionally normalized to total. Original blot in Source Data **c**. **b**, Heatmap of glucose transporter expression relative to *SLC2A1* in HAECs captured by qRT-PCR (n = 3 biological replicates) **c-d**, Western blot of SLC2A1, SLC2A3, phospho-cofilin and phospho-MLC in the presence or absence of two distinct siRNA (separate from the one used in Fig. 5a) (#1 in **c** and #2 in **d**) targeted towards SLC2A3 and thrombin treatment (n = 3 biological replicates. For **c**, $P = 0.0190$ for pCFL and 0.0490 for ppMLC. For **d**, $P = 0.0272$ for ppMLC.). Loading control for each protein is ACTB unless specifically denoted in parentheticals. Phospho-proteins are additionally normalized to total. Original blot in Source Data **d-e. e**, Single-cell LPR of HAECs treated with thrombin in the presence of si*SLC2A1* or si*SLC2A3* (n = 277 for thrombin vs. control, n = 281 for thrombin vs. thrombin + si*SLC2A1*, and n = 278 for thrombin vs. thrombin + si*SLC2A3*, $P < 0.0001$, $P = 0.0384$, $P < 0.0001$, respectively.). **f-g**, Glucose (**f**) and ATP levels (**g**) in single-cells in the presence or absence of *SLC2A3* knockdown and thrombin treatment (**f**: n = 248, 248, 108, 190 from left to right, $P < 0.0001$ for all comparisons; **g**: 190, 598, 150, 287 from left to right, $P < 0.0001$ for all comparisons). **h**, Gap index of cells treated with or without thrombin in the presence or absence of *SLC2A3* knockdown (n= 12, 16, 8, 32 from left to right). **i-j**, Representative images of HAECs treated with si*SLC2A3* or control with varying concentrations of glucose (**i**) or with oligomycin (**j**) in the presence of thrombin. Red color is CDH5. Gap size index and gap index quantification of images (**i**, n = 10, 10, 7, 8 from left to right, p = 0.022 for gap size index and $P = 0.0019$; **j**, n = 6 for gap size index, $P = 0.0013$ for si*SLC2A3* vs control and $P = 0.040$ for si*SLC2A3* vs. si*SLC2A3* + oligomycin, and n = 10, 11, 7 from left to right for gap index, $P < 0.0001$). White stars highlight gaps in the monolayer. Scale bars = 250 μm. Statistical significance determined by multiple unpaired two-tailed t-tests (**a**, **c**, **d**), one-way ANOVA followed by Bonferroni test (**e-g, i**) or by two-sided Welch's t-test (**h, j**). All error bars are s.e.m. $^{*}P <= 0.05$; $^{**}P <= 0.005$; $^{***}P <= 0.0005$.

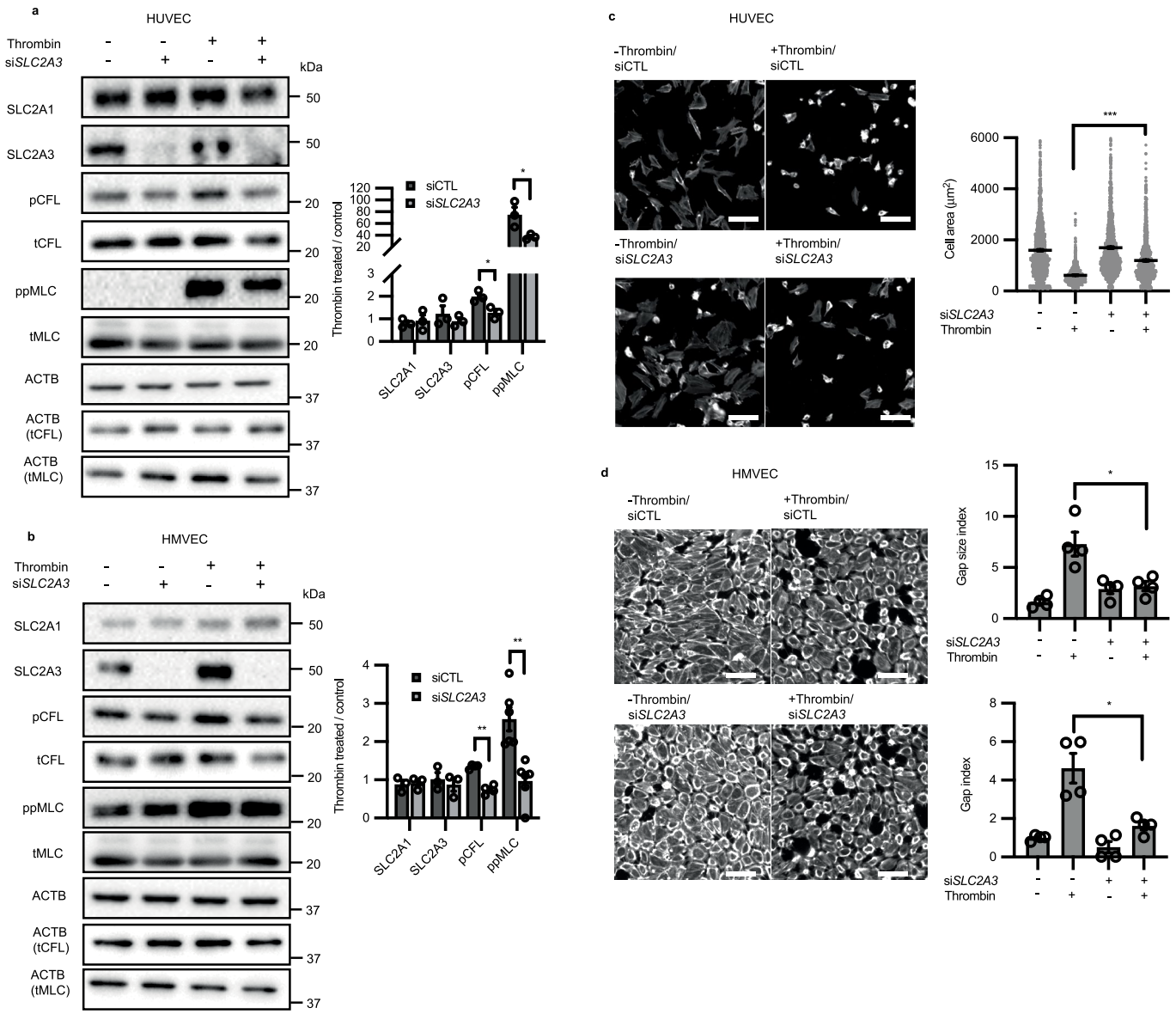

Extended Data Fig. 5 | SLC2A3 inhibition abrogates thrombin-induced phosphorylation of CFL and MLC and contraction across multiple endothelial cell types. a-b, Western blot analysis of glucose transporter expression, phosphorylated CFL, and phosphorylated MLC, in human umbilical vein endothelial cells (HUVEC, **a**, n = 3; biological replicates, $P = 0.0257$ for pCFL and 0.0414 or ppMLC) and human microvascular endothelial cells (HMVEC, **b**, n = 3 for SLC2A1, SLC2A3, n = 4 for CFL and n = 5 for MLC; biological replicates, $P < 0.001$ for pCFL and $P = 0.0014$ for ppMLC). Loading control for each protein is ACTB unless specifically denoted in parentheticals. Original blot in Source Data **f-g. c**, Representative images and cell size of contractile HUVECs subjected to thrombin stimulation in the absence or presence of SLC2A3 knockdown. (n = 1375, 1279, 760, 1162 from left to right, $P < 0.0001$) **d**, Representative images, gap size index, and gap index of contractile HMVECs subjected to thrombin stimulation in the absence or presence of *SLC2A3* knockdown. Representative images are phalloidin. (n = 4 biological replicates, $P = 0.0171$ for gap size index and $P = 0.0262$ for gap index) Statistical significance determined by two-sided Welch's t-test. All error bars are s.e.m. n.s., not significant. *P <= 0.05; **P <= 0.005; ***P <= 0.0005.

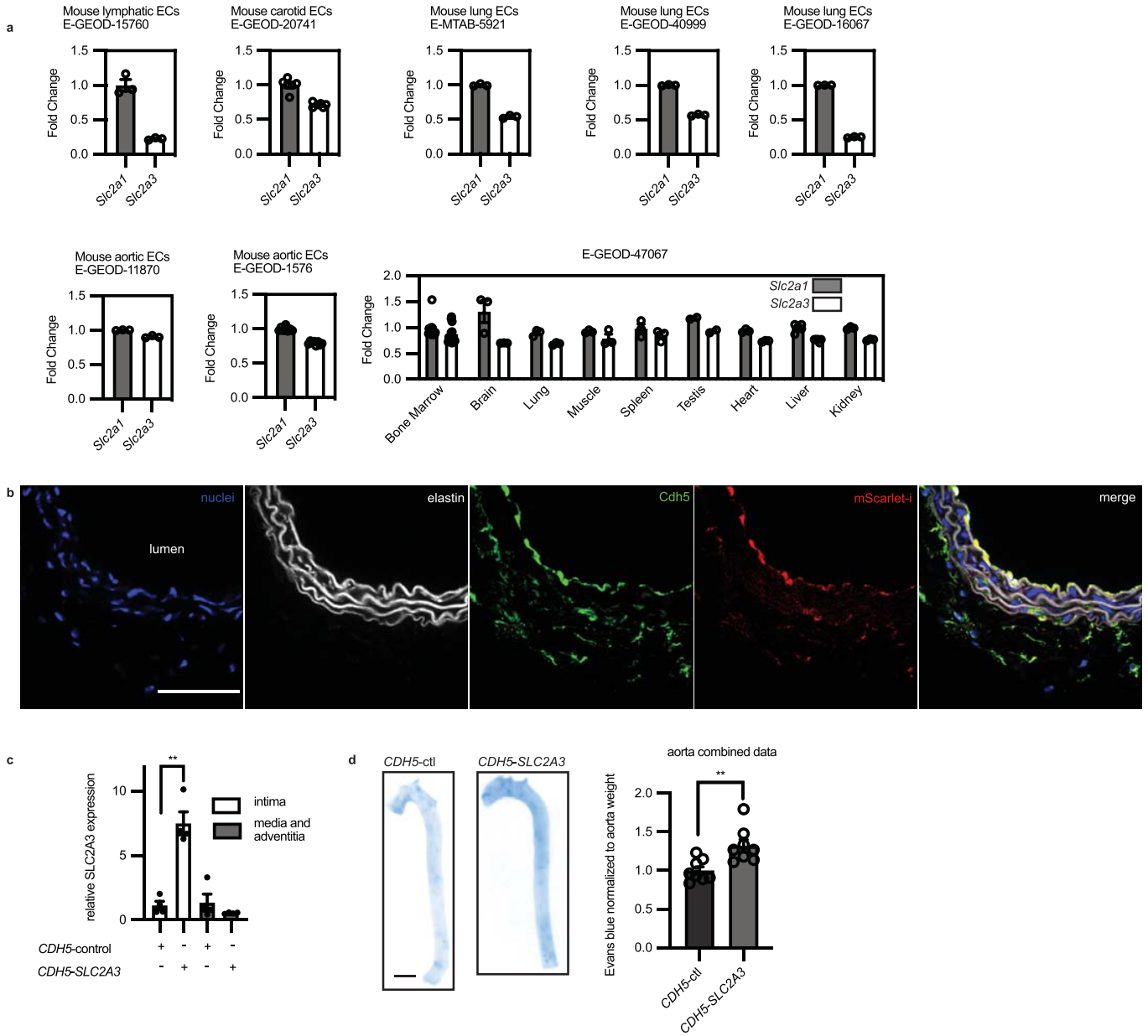

Extended Data Fig. 6 | In vivo overexpression of *SLC2A3* increased vascular leak. a, GEO datasets of primary endothelial mouse cells comparing *Slc2a1* and *Slc2a3* from different organs. Fold change indicates that data are normalized to *Slc2a1* except for E-GEOD-47067 which was normalized to average of *Slc2a1* in all tissues. Only controls of experiments in the GEO datasets were used in these analyses. (n = 3 independent biological replicates for each condition for E-GEOD-15760; n = 6 independent biological replicates for each condition for E-GEOD-20741; n = 3 independent biological replicates for each condition for E-MTAB-5921; n = 3 independent biological replicates for each condition for E-GEOD-40999; n = 3 independent biological replicates for each condition for E-GEOD-11870; n = 3 independent biological replicates for each condition for E-GEOD-1576; n = 3 independent biological replicates for condition in each organ for E-GEOD-47067) **b**, Immunofluorescence of an arterial section demonstrating enhanced mScarlet-i fluorescence (red) colocalized with ve-cadh (green) which marks the endothelium next to the lumen (yellow, merge) (Scale bar, 500 µm, representative of n = 4 mice). **c**, *SLC2A3* expressing plasmid uses an endothelial specific CDH5 promoter. *SLC2A3* is detected by qRT-PCR of the intima of the mouse aorta, and far less than in the media and adventitia. (n = 4 independent biological replicates, $P = 0.0030$) **d**, Evans blue (OD 620 nm) quantification of mouse aortas, normalized by weight. (n = 8 independent biological replicates for each condition, $P = 0.0050$). Scale bar is 1 mm. Statistical significance was determined by two-sided Welch's t-test. All error bars are s.e.m. $^{**}P <= 0.005$.

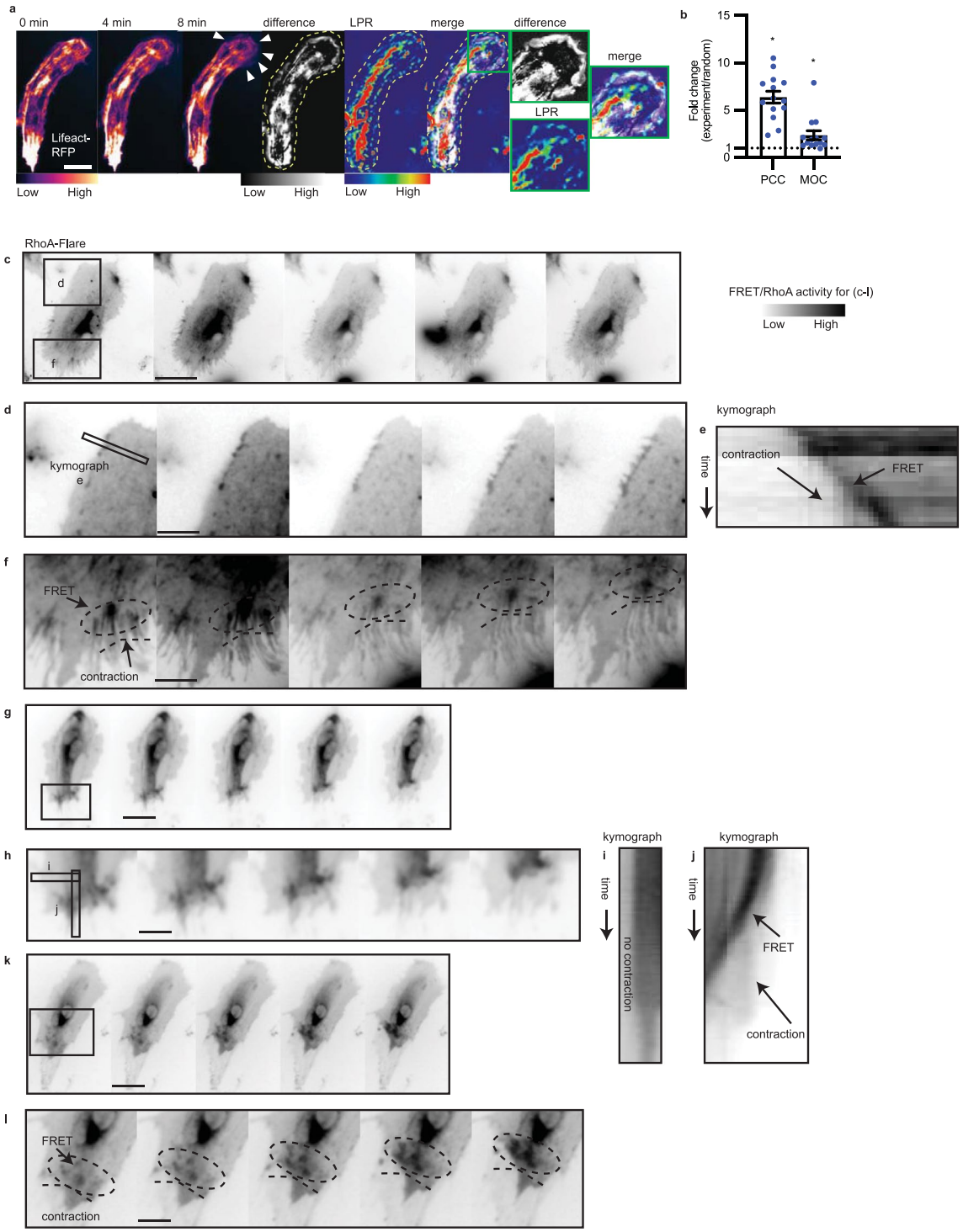

Extended Data Fig. 7 | Subcellular RhoA activity, actin turnover, and LPR distribution in single motile endothelial cells. a, Montage of actin timelapse in a migratory endothelial cell; maximum projection of change in actin structure (Lifeact difference image, obtained by sequential subtraction of preceding 10 images, taken 1 minute apart, followed by maximum intensity projection of the absolute value of the differences), per pixel LPR map (LPR), Lifeact difference and LPR overlap ("difference+LPR", merge), scale bar = 20 μm. White arrows in montage indicate cell spreading. Green outline shows enhanced LPR near the regions of cell spreading. Representative of n = 14 cells, 3 separate experiments. **b**, Pearson's correlation coefficient (PCC) and Manders' overlap coefficient (MOC) of Lifeact difference and LPR, compared to random. The random PCC/MOC is calculated by randomizing the LPR image and computing with the Lifeact difference image. Fold change of experimental PCC/MOC over randomized is shown. (n = 14). Error bars are s.e.m, $P = 0.014$ for PCC and $P = 0.0489$ for MOC. **c-l**, RhoA activity measured by RhoA-FLARE in contractile endothelial cells. Representative data of total n = 9 cells in 3 replicates. (Scale bar = 16 μm in **c**, **g**, **k**. Scale bar = 7 μm in **d**, **f**, **h**, **l**). **d**,**f**, regions of contractile cell from (**c**) showing RhoA membrane activity. Circle in (**f**) notes moving RhoA activity. **e**, kymograph showing contractile edge from (**d**) and increasing RhoA activity over time. **h**, region of contractile cell from (**g**) showing increased RhoA membrane activity. **i-j**, kymograph showing non-contractile edge (**i**) without RhoA increase and contractile edge (**j**) from (**g**) and increasing RhoA activity over time. **l**, region of contractile cell from (**k**) showing RhoA membrane activity. Dotted ellipses notes highlight increasing RhoA activity along with active contraction. Statistical significance determined by two-sided Welch's t-test. *P <= 0.05.

nature research

Corresponding author(s): Yun Fang, Jun Huang

Last updated by author(s): Mar 26, 2021

Reporting Summary

Nature Research wishes to improve the reproducibility of the work that we publish. This form provides structure for consistency and transparency in reporting. For further information on Nature Research policies, see our Editorial Policies and the Editorial Policy Checklist.

Statistics

For all statistical analyses, confirm that the following items are present in the figure legend, table legend, main text, or Methods section.

n/a	Confirmed	
☐	☒	The exact sample size (*n*) for each experimental group/condition, given as a discrete number and unit of measurement
☐	☒	A statement on whether measurements were taken from distinct samples or whether the same sample was measured repeatedly
☐	☒	The statistical test(s) used AND whether they are one- or two-sided *Only common tests should be described solely by name; describe more complex techniques in the Methods section.*
☒	☐	A description of all covariates tested
☐	☒	A description of any assumptions or corrections, such as tests of normality and adjustment for multiple comparisons
☐	☒	A full description of the statistical parameters including central tendency (e.g. means) or other basic estimates (e.g. regression coefficient) AND variation (e.g. standard deviation) or associated estimates of uncertainty (e.g. confidence intervals)
☐	☒	For null hypothesis testing, the test statistic (e.g. *F*, *t*, *r*) with confidence intervals, effect sizes, degrees of freedom and *P* value noted *Give P values as exact values whenever suitable.*
☒	☐	For Bayesian analysis, information on the choice of priors and Markov chain Monte Carlo settings
☒	☐	For hierarchical and complex designs, identification of the appropriate level for tests and full reporting of outcomes
☒	☐	Estimates of effect sizes (e.g. Cohen's *d*, Pearson's *r*), indicating how they were calculated

Our web collection on statistics for biologists contains articles on many of the points above.

Software and code

Policy information about availability of computer code

Data collection	All images were collected with MicroManager v1.4
Data analysis	All statistical tests were performed in Prism 9.0. CellProfiler 3.0.0 was used for generation of ground truth images. All image analysis was performed using Matlab version R_2018b with custom code available at https://github.com/wulab-code/laconic. ImageJ v2.0.0 was used to process Western Blots.

For manuscripts utilizing custom algorithms or software that are central to the research but not yet described in published literature, software must be made available to editors and reviewers. We strongly encourage code deposition in a community repository (e.g. GitHub). See the Nature Research guidelines for submitting code & software for further information.

Data

Policy information about availability of data

All manuscripts must include a data availability statement. This statement should provide the following information, where applicable:

- Accession codes, unique identifiers, or web links for publicly available datasets
- A list of figures that have associated raw data
- A description of any restrictions on data availability

Gene Expression Omnibus datasets (GEOD) were downloaded from EndoDB (https://endotheliomics.shinyapps.io/endodb/): E-GEOD-15760, E-GEOD-20741, E-MTAB-5921, E-GEOD-40999, E-GEOD-16067, E-GEOD-11870, E-GEOD-1576, E-GEOD-47067. Original data that supports our findings in this study is available from the corresponding author upon reasonable request or at doi:10.5281/zenodo.4638059.

Field-specific reporting

Please select the one below that is the best fit for your research. If you are not sure, read the appropriate sections before making your selection.

☒ Life sciences ☐ Behavioural & social sciences ☐ Ecological, evolutionary & environmental sciences

For a reference copy of the document with all sections, see nature.com/documents/nr-reporting-summary-flat.pdf

Life sciences study design

All studies must disclose on these points even when the disclosure is negative.

Sample size	For imaging, sample sizes were chosen based on the number of cells in a given field of view and the available field of views per sample. We deemed this to be sufficient in our studies since the values of each condition formed a normal distribution and are reproducible across multiple experiments. For western blots, we maximized the sample size based on the available number of lanes in the gel. Again, our findings were reproducible across multiple replicates.
Data exclusions	No data were excluded from analysis unless there were frank technical errors such as poor Western Blot transfers or loading errors.
Replication	Each experiment was replicated or performed independently as described in the figure legend.
Randomization	Samples and organisms (mice) were randomly assigned to a treatment group. For mixing experiments, randomization was performed by mixing samples to be evaluated together then deconvolution based on color as in Figure 1.
Blinding	Data collection was blinded to sample treatment/group allocation. Data analysis (single cell analysis and gap size) was also blinded to sample treatment/group allocation; results were assigned sample/group labels only after data analysis was completed. Blinding is not relevant to Western Blot experiments as samples need to be loaded in correct order on gels.

Reporting for specific materials, systems and methods

We require information from authors about some types of materials, experimental systems and methods used in many studies. Here, indicate whether each material, system or method listed is relevant to your study. If you are not sure if a list item applies to your research, read the appropriate section before selecting a response.

Materials & experimental systems

n/a	Involved in the study
☐	☒ Antibodies
☐	☒ Eukaryotic cell lines
☒	☐ Palaeontology and archaeology
☐	☒ Animals and other organisms
☒	☐ Human research participants
☒	☐ Clinical data
☒	☐ Dual use research of concern

Methods

n/a	Involved in the study
☒	☐ ChIP-seq
☒	☐ Flow cytometry
☒	☐ MRI-based neuroimaging

Antibodies

Antibodies used	Antibodies for immunofluorescence: SLC2A3 (R&D Systems, MAB1415, 12.5 µg/mL, clone #202017), CDH5/VE-CADH (Cell Signaling, 2500S, 1:250 dilution). Antibodies for Western blot: SLC2A3 (ProteinTech, 20403-1-AP, 1:1000 dilution), SLC2A1 (ProteinTech, 21829-1-AP, 1:1000), pCFL (Cell Signaling, 3313T, 1:1000 dilution), tCFL (Cell Signaling, 5175T, 1:1000 dilution), ppMLC (Cell Signaling, 3674S, 1:1000 dilution), tMLC (Sigma, M4401, 1:1000 dilution, clone #MY-21), ACTB (Abcam, ab6276, 1:1000 dilution, clone #AC-15). Secondary antibodies: anti-Mouse IgG-HRP (Calbiochem 401253, 1:3000) or anti-Rabbit IgG-HRP (Cell Signaling 7074S, 1:5000). Alexa Fluor 594 Goat Anti-Mouse IgG (Life Technologies, A11037, 1:1000), Alexa Fluor 488 Goat Anti-Rabbit IgG (Life Technologies, A11034, 1:1000).
Validation	SLC2A3 (R&D Systems, MAB1415, 12.5 µg/mL) was validated for human cells according to the manufacturer: Detects human Glut3; Recognizes human Glut3 expression on human Glut3-transfected NS0 cells, but not the NS0 control transfectants; No cross-reactivity was observed with transfectants expressing human Glut1 or human Glut2. Relevant citation (doi): 10.1073/pnas.1800525115, 10.3324/haematol.2018.205724, 10.1530/EJE-07-0532. CDH5/VE-CADH (Cell Signaling, 2500S, 1:250 dilution) has been validated for use on human cells and tissue for immunofluorescence according to the manufacturer: VE-Cadherin (D87F2) XP® Rabbit mAb recognizes endogenous levels of total VE-cadherin protein; The antibody does not cross-react with other cadherin family proteins. Relevant citations (doi): 10.1172/JCI84876, 10.3892/ol.2015.3752. SLC2A3 (ProteinTech, 20403-1-AP, 1:1000 dilution) has been validated for use in human cells (HEK-293 cells, C6 cells, HeLa cells,

Jurkat cells, mouse brain tissue, U-251 cells) for western blot according to the manufacturer. We verified SLC2A3 specific labeling using siRNA knockdown in HAEC in Extended Data Figure 4c and 4d. Relevant citations (doi): 10.1080/15548627.2019.1580105, 10.1016/j.celrep.2020.107877, 10.1016/j.ygcen.2015.01.017.

SLC2A1 (ProteinTech, 21829-1-AP, 1:1000) has been validated for use in human cells (Y79 cells, HEK-293 cells, NIH/3T3 cells, SH-SY5Y cells) for western blot according to the manufacturer. We verified SLC2A1 specific labeling using siRNA knockdown in HAEC in Extended Data Figure 4a. Relevant citations: 10.1096/fj.201802226R, 10.1158/0008-5472.CAN-18-3842, 10.1038/s41467-019-08618-y.

pCFL (Cell Signaling, 3313T, 1:1000 dilution) has been validated for use in human cells for western blot according to manufacturer: Phospho-Cofilin (Ser3) (77G2) Rabbit mAb detects endogenous levels of cofilin only when phosphorylated at serine 3. Relevant citations (doi): 10.1038/s41419-019-1497-1, 10.1242/jcs.205393, 10.1038/s41467-017-00111-8.

tCFL (Cell Signaling, 5175T, 1:1000 dilution) has been validated for use in human cells for western blot according to manufacturer: Cofilin (D3F9) XP® Rabbit mAb detects endogenous levels of total cofilin1 protein. Relevant citations (doi): 10.3390/ijms20225647, 10.1038/s41419-019-1497-1, 10.1016/j.tranon.2018.03.003.

ppMLC (Cell Signaling, 3674S, 1:1000 dilution) has been validated for use in human cells for western blot according to the manufacturer: Phospho-Myosin Light Chain 2 (Thr18/Ser19) Antibody detects endogenous levels of myosin light chain 2 only when dually phosphorylated at threonine 18 and serine 19; The antibody does not cross-react with the cardiac isoform of myosin light chain 2. Relevant citations (doi): 10.1167/iovs.17-23702, 10.18632/oncotarget.22370, 10.1083/jcb.201703107.

tMLC (Sigma, M4401, 1:1000 dilution) has been validated for use in human cells for western blot according to the manufacturer. Relevant citations (doi): 10.1152/ajpregu.00717.2003, 10.1161/01.res.82.5.594, 10.1111/j.1476-5381.2009.00591.x.

ACTB (Abcam, ab6276, 1:1000 dilution) has been validated for use in human cells for western blot according to the manufacturer. Relevant citations (doi): 10.26508/lsa.201900542, 10.1016/j.omtn.2019.10.026, 10.1186/s13578-020-00422-2.

Eukaryotic cell lines

Policy information about cell lines

Cell line source(s)	Lonza (HAEC and HUVEC); Promocell (HMVEC)
Authentication	Cell lines were identified to by endothelial by CD31 expression by the vendor.
Mycoplasma contamination	All cell lines were tested negative for mycoplasma contamination.
Commonly misidentified lines (See ICLAC register)	Not used

Animals and other organisms

Policy information about studies involving animals; ARRIVE guidelines recommended for reporting animal research

Laboratory animals	Mouse (Mus Musculus): C57BL/6J, 10-12 week old, male and female. All experimental animals were maintained in a pathogen-free environment with a humidity of 40-60%, a temperature of 20–24°C, and a 12-h light/dark cycle at the University of Chicago.
Wild animals	This study did not involve wild animals.
Field-collected samples	This study did not involve field-collected samples.
Ethics oversight	All animal care and treatment procedures were approved by the University of Chicago Institutional Animal Care and Use Committee. Animals were handled according to the National Institutes of Health Guide for the Care and Use of Laboratory Animals and all experiments were compliant with ethical guidelines from The Guide for the Care and Use of Laboratory Animals.

Note that full information on the approval of the study protocol must also be provided in the manuscript.